Nano Research

Open Access

Research Article

In-situ dynamic activation promotes the synergy between adsorbate evolution and lattice oxygen mechanisms for efficient water oxidation

Bo Li[1,§] ✉, Yu-Han Wang[2,§], Tao Huang[2], Lei Li[2], Qian Fang[1], Jinghui Shi[2], Gui-Fang Huang[2] ✉, Wangyu Hu[3], and Wei-Qing Huang[2] ✉

[1] *College of Electronic and Electrical Engineering, Shangqiu Normal University, Shangqiu 476000, China*
[2] *College of Physics and Electronics, Hunan University, Changsha 410082, China*
[3] *College of Materials Science and Engineering, Hunan University, Changsha 410082, China*
[§] *Bo Li and Yu-Han Wang contributed equally to this work.*

Cite this article: *Nano Research*, **2026**, *19*, 94908466. https://doi.org/10.26599/NR.2026.94908466

ABSTRACT: The synergistic activation of metal and lattice oxygen in transition metal-based catalysts through adsorbate evolution mechanism (AEM) and lattice oxygen mechanism (LOM) is regarded as one of the key strategies for boosting oxygen evolution reaction (OER) activity and stability, but still remains challenge. Herein, leveraging an *in-situ* electrochemical activation, we reveal that the designed bimetallic phosphide heterojunction is dynamically activated into coexisting phosphides and hydroxides active phases, each following the AEM and LOM pathways respectively. Specifically, Ni atoms at the dense NiFeP@FeP heterointerfaces effectively tune the rate-determining step (RDS) (OH* to O*) energy barrier under the AEM pathway, while the interface interaction in NiFeP-NiFe layer double hydroxide (LDH) weakens the metal–O bond and lowers the d-band center of metal sites, enabling effective LOM pathway. *In-situ* spectroscopy combined with ^{18}O-isotopic labelling and differential electrochemical mass spectrometry (DEMS) measurements revealed dynamic reconfiguration and both involved adsorbed/lattice oxygen signature products in the oxygen release process, affirming the synergy of AEM-LOM pathway. As a result, the activated catalyst only requires overpotentials of 197/233 mV to drive current densities of 10/100 mA·cm^{-2}, accompanied by Tafel slope of 32 mV·dec^{-1} and turnover frequency (TOF) value of 0.05 s^{-1}, as well as high stability for OER. This work provides insights for deeper understanding of the OER mechanism of transition metal phosphides and the design of high efficient catalysts.

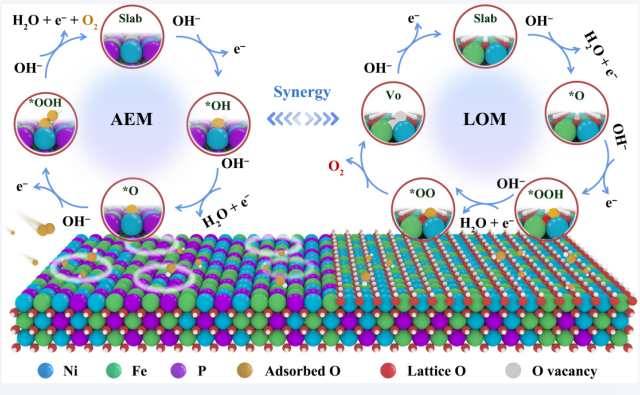

KEYWORDS: transition-metal phosphides, heterostructure, *in-situ* activation, adsorbate evolution mechanism (AEM)/lattice oxygen mechanism (LOM), oxygen evolution

1 Introduction

Hydrogen energy is an ideal alternative for fossil fuel and becomes a hot research topic in the scientific community [1–5]. Electrochemical water splitting, including two half reactions, namely oxygen evolution reaction (OER) and hydrogen evolution reaction (HER), is one of the most attractive methods to produce low-price and highly purified hydrogen [6–9]. The anodic OER, which proceeds through 4e$^-$ transfer and generates multiple intermediates (*OH, *O, and *OOH) is much more kinetically sluggish than HER, thus limiting the overall efficiency and practical applications [10–12]. Consequently, a fundamental understanding of the OER catalysis mechanism is of great significance for designing and preparing advanced catalysts to overcome the challenges of high overpotential and slow kinetics.

Considering the different pathways of O–O bond formation, two

Received: September 23, 2025; **Revised:** December 31, 2025
Accepted: January 21, 2026

✉Address correspondence to Bo Li, boli1993@hnu.edu.cn; Gui-Fang Huang, gfhuang@hnu.edu.cn; Wei-Qing Huang, wqhuang@hnu.edu.cn

mechanisms have typically been accepted for OER, i.e., the adsorbate evolution mechanism (AEM) and lattice oxygen mechanism (LOM) [13–17]. Catalysts following the traditional AEM involve only the adsorption and desorption of reactants, where the electronic states near the Fermi level exhibit metallic properties and the metal site serves as redox center (Fig. 1(a)). Since the catalytic activity toward AEM pathway is determined by the adsorption energy of the O-containing intermediates (*OH, *O, and *OOH), the difference in Gibbs free energy between the breakage of the O–H bond and the formation of the *OOH bond is approximately 3.2 eV ($\Delta G_{*OOH} - \Delta G_{*OH}$), resulting in the minimum intrinsic overpotential limitation of OER being 370 mV [18–20]. For the LOM, where the electronic states near the Fermi level are occupied by oxygen (Fig. 1(b)), and the lattice oxygen acts as the redox center [21]. Bracingly, the LOM-based OER process has been proposed to overcome the limitations of Sabatier's principle and linear-scaling relationship, as it achieves directly O–O coupling without generating the *OOH intermediate [22–24]. Recently, we have demonstrated that the LOM mechanism can be effectively activated through the photogenerated hole oxidation of metal species and the regulation of oxygen vacancy concentration methods, thereby significantly improving the OER performance [25, 26]. So far, the research on the LOM pathway of the OER has provided valuable insights for the design of advanced catalysts, such as (La, Sr)$CoO_{3-\delta}$ [21], CoZn (oxy)hydroxide [27], NiFeP [28], and NiFe (oxy)hydroxide [29]. However, several challenging issues regarding the LOM pathway of OER catalysts remains: (i) The participation of lattice oxygen will trigger a dynamic equilibrium between the formation and filling of oxygen vacancies, resulting in the gradual structural turbulence of the catalyst [30–32]. (ii) According to the Pourbaix diagram, thermodynamic barriers impose restrictions on the oxidation cycle of the currently widely used 3d transition metal-based catalysts due to that the highly oxidized metal species usually requires more elevated overpotential,

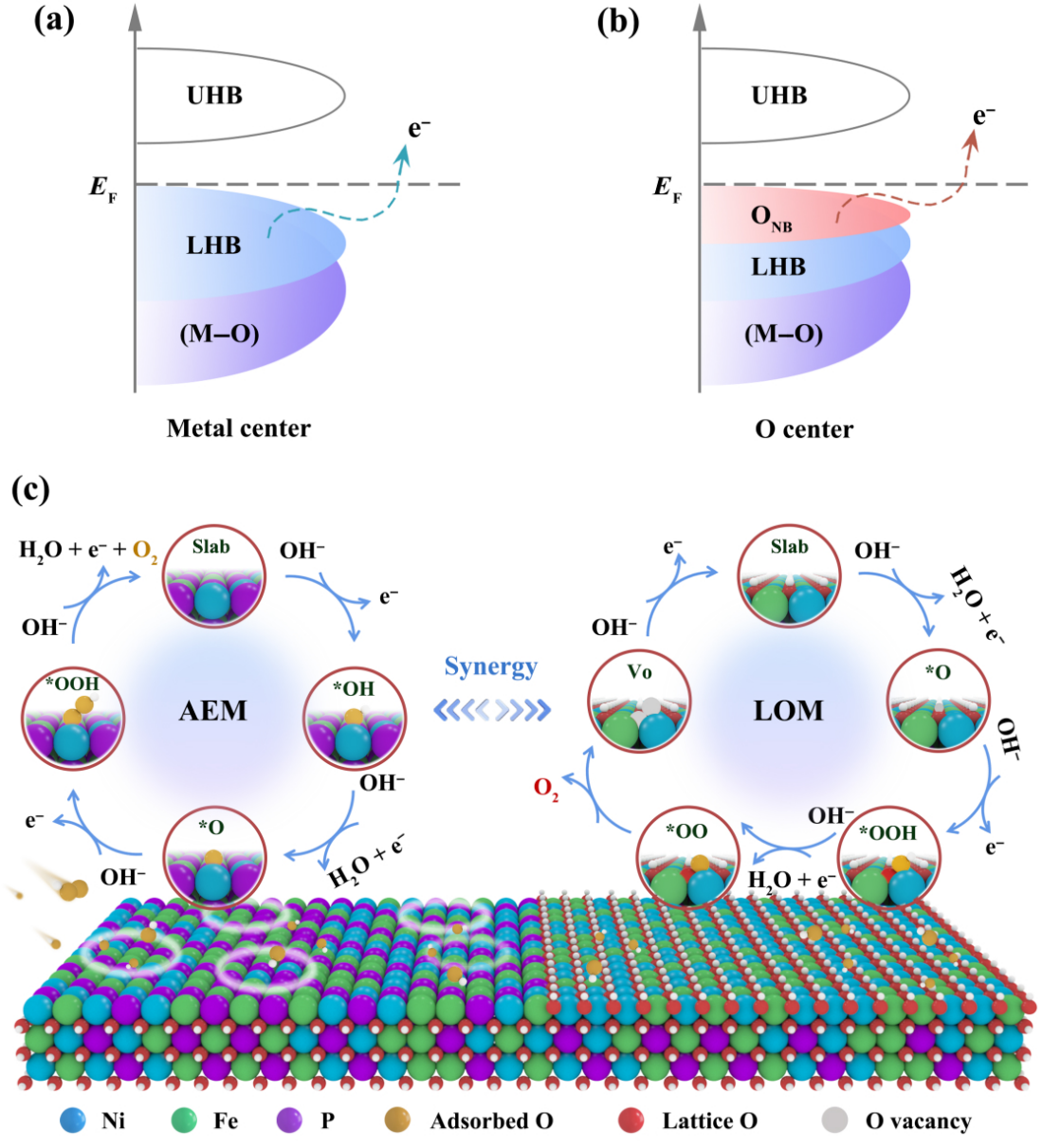

Figure 1 (a) and (b) Illustration of currently two OER mechanisms: the AEM of metals as redox centers and the LOM of oxygen as a redox center. (c) Schematic illustration of *in-situ* dynamic activated AEM and LOM synergistic mechanism on nickel-iron phosphide heterostructures.

thereby causing unfavorable activity [19, 33]. (iii) The dominant LOM pathway cannot fully utilize the active sites of the catalyst, especially the metal sites exposed on the surface [34]. Undoubtedly, these unfavorable factors have made the LOM pathway difficult to predict and have hindered the development of high efficient OER catalysts. Thus, we can expect that a rational design of the AEM-LOM synergistic mechanism that simultaneously utilizes the metal and lattice oxygen active sites will provide a promising avenue for effectively integrating the advantages of each reaction pathway and maximizing the efficiency and stability of the OER.

Given by the above consideration, we herein report an *in-situ* dynamic activation strategy to facilitate the synergy of the AEM and LOM pathway (Fig. 1(c)). The transition-metal phosphides embedded heterostructures that consist of ultrathin NiFeP nanosheets and chemically embedded FeP nanodots (named as NiFeP NSs@FeP NDs) as pre-catalyst, which can undergo dynamically phase transition of the surface active sites from complete phosphide to incomplete layered double-hydroxide and (oxy)hydroxide during *in-situ* oxidizing OER process with increasing applied overpotential. Our *in-situ* and *ex-situ* experimental investigations reveal that the evolution of active sites and intermediates on incompletely transformed phosphides-(oxy)hydroxides enables activation of both metal and lattice oxygen sites. Density functional theory (DFT) calculations indicate that Ni atoms on the unique interface coordination environments between NiFeP and FeP greatly reduce the electrochemical reaction barrier via tuning the formation processes of O* and OOH* under the AEM pathway, and the interface interaction in NiFeP-NiFe layer double hydroxide (LDH) weakens the bond strength between metal and O atoms, as well as lowers the d-band center of metal sites, enabling effective LOM pathway at the Ni-Fe dual-site and further improving the OER kinetics. As a result of the synergy of the AEM-LOM, in this case, the optimized catalyst displays excellent OER performance with 197 and 233 mV overpotentials at 10 and 100 $mA{\cdot}cm^{-2}$ in 1.0 M KOH electrolyte.

2 Experimental section

2.1 Chemicals and reagents

Chemicals and materials were purchased from the following suppliers: Ni foam (1.7 mm in thickness, Taiyuan Lizhiyuan Science and Technology Co., China), hydrochloric acid (Sinopharm Chemical Reagent Co., China), acetone (Sinopharm Chemical Reagent Co., China), ethanol (Tianjin Zhiyuan Chemical Reagent Co., China), $Fe(NO_3)_3{\cdot}9H_2O$ (Sinopharm Chemical Reagent Co., China), $Ni(NO_3)_2{\cdot}6H_2O$ (Sinopharm Chemical Reagent Co., China), and KOH (Sinopharm Chemical Reagent Co., China). All chemicals and materials were used as received without further purification.

2.2 Pretreatment of nickel foam (Ni foam) substrates

A piece of Ni foam was sonicated with concentrated hydrochloric acid, acetone, ethanol, and deionized water for 10 min. After sonication, the resultant material was taken out and rinsed repeatedly with copious deionized (DI) water.

2.3 Synthesis of NiFe LDHs@FeOOH arrays

The Ni foam was immersed in a mixing aqueous solution (3 mL) containing of $Fe(NO_3)_3{\cdot}9H_2O$ (0.5 mmol) and $Ni(NO_3)_2{\cdot}6H_2O$ (1 mmol), which was heated in an oven (60 °C) for 5 h, and then the obtained bulk $NiFe(OH)_3$ sample was taken out and rinsed repeatedly with DI water. After that, the above $NiFe(OH)_3$ was immersed into KOH solution (30 mL, 1.0 M) and hydrothermally treated at 120 °C for 12 h. After cooling to room temperature, the sample was taken out and repeatedly washed with DI water and dried.

2.4 Synthesis of NiFeP NSs@FeP NDs heterostructure

Firstly, the NiFe LDHs@FeOOH arrays and NaH_2PO_2 (0.2 g) were placed in two separate porcelain boats with NaH_2PO_2 at the upstream side of the tube furnace. Subsequently, the samples were annealed at 300 °C for 140 min with a ramp rate of 2 $°C{\cdot}min^{-1}$ under a flow of Ar gas, and then cooled to ambient temperature under Ar atmosphere.

2.5 Synthesis of bare NiP and FeP

The samples were prepared by a method similar to that for the NiFeP NSs@FeP NDs in the absence of $Fe(NO_3)_3$ or $Ni(NO_3)_2$, respectively.

2.6 Material characterization

X-ray diffractometry (XRD) measurements was performed on a Siemens D-5000 diffractometer with Cu-Kα radiation (λ = 0.154 nm). Scanning electron microscopy (SEM) measurements and energy dispersive X-ray spectroscopy (EDS) elemental mapping measurements were performed on a field emission scanning electron microscopy (Hitachi S-4800, equipped with energy dispersive X-ray detector). Transmission electron microscope (TEM), and high-resolution TEM (HRTEM) were performed on a transmission electron microscope (JEM-3010, Japan). X-ray photoelectron spectroscopy (XPS) was conducted by a PHI Quantera X-ray photoelectron spectrometer with an Al Kα source (300 W). The nanosheets grown on the Ni foam were detached by ultrasound, and then evenly distributed on the Si wafer by spin coating, the corresponding thickness was measured by atomic force microscopy (AFM) carried out on a Park Systems Crop scanning probe microscopy system (Lui-Dong 906-10, Suwon, Republic of Korea). The specific surface area was calculated using the Brunauer–Emmett–Teller (BET) method from adsorption data recorded using the Quabrasorb SI-3MP. The oxygen vacancy was characterized by electron paramagnetic resonance (EPR, Bruker Emxplus, Germany). The element analysis of the samples was identified and evaluated using an inductively coupled plasma optical emission spectrometer (ICP-OES, Agilent 725ES).

2.7 Electrochemical measurements

All OER tests were performed on a CHI660E workstation in a three-electrode system using the as-synthesized catalysts, Pt wire, and Ag/AgCl electrode in saturated KCl solution as the working, counter, and reference electrodes, respectively. 1.0 M KOH with saturated O_2 was applied as the electrolyte. The loading mass of NiFeP NSs@FeP NDs was determined to be 2.0 $mg{\cdot}cm^{-2}$ by weighing the Ni foam before and after loading. For comparison samples, in order to ensure that the loading mass of the catalysts is the same as that of NiFeP NSs@FeP NDs, the prepared samples (such as FeP) were subjected to ultrasonic treatment at different intervals. After drying treatment, samples with target loading mass were screened by weighing for the next test. Similarly, the same amount of commercial catalysts (IrO_2/C, IrO_2) were loaded on Ni

foam for comparison. The linearsweep voltammetry (LSV) polarization curves were conducted at a rate of 2 mV·s^{-1} in O_2-saturated 1.0 M KOH solution with the *iR* compensations. The electrochemical impedance spectroscopy (EIS) measurements were carried out in the frequency range from 1 MHz to 0.05 Hz. The chronopotentiometry was carried out under a constant current density of 10 mA·cm^{-2} in O_2-saturated 1.0 M KOH solution.

The Tafel slope was calculated according to the following equation: $\eta = b^*\log|j| + a$, where η is the overpotential (V), j is the current density (mA·cm^{-2}), and b is the Tafel slope (mV·dec^{-1}). The C_{dl} was calculated by performing CV measurements at different scan rates of 10, 20, 30, 40, 50, 60, 70, 80, 90, and 100 mV·s^{-1}. The value of C_{dl} was a half of the linear slope obtained from plotting $\Delta j = j_a - j_c$ against the scan rates (j_a and j_c are anode and cathode current density, respectively). All the potentials were calibrated to the reversible hydrogen electrode (vs. RHE), and the corresponding equation is $E_{RHE} = E_{Ag/AgCl} + 1.026$ V. The OER Faraday efficiency was determined in 1.0 M KOH with a NiFeP NSs@FeP NPs as the working electrode via a drainage method in a fully enclosed H reaction cell with a standard three-electrode system. First, the gas collection bottle filled with water in the water tank was inverted, when continuous and uniform bubbles appear at the gas-guide tube mouth, then the nozzle was extended into the inside of the collecting bottle mouth, and a certain volume of water expelled corresponded to the volume of oxygen collected.

2.8 Electrochemical *in-situ* Raman spectra measurements

Electrochemical *in-situ* Raman spectra were recorded with a confocal Raman microscope (Renishaw inVia Reflex spectrometer) using a 532 nm laser for the analysis. The Raman frequencies were corrected using silicon wafer. The *in-situ* electrochemical cell was composed of obtained samples, platinum wire, and Ag/AgCl electrode in saturated KCl solution, serving as working, counter, and reference electrode, respectively. To monitor the evolution of catalyst samples during OER process, Raman spectrum was collected after a constant potential was applied to the catalyst electrode for 10 min. Each Raman spectrum was obtained by the integration time of 10 s with accumulating 5 times.

2.9 Electrochemical *in-situ* Fourier transform infrared (FTIR) spectra measurements

Electrochemical *in-situ* Fourier transform infrared spectroscopy (Bruker VERTEX 70 V) was carried out by using a three-electrode setup in 1.0 M KOH. The electrochemical cell was composed of samples, platinum wire, and Ag/AgCl electrode in saturated KCl solution, serving as working, counter, and reference electrode, respectively. FTIR measurements were performed under steady-state conditions at a fixed potential.

2.10 ^{18}O-labeling and differential electrochemical mass spectrometry (DEMS) measurements

NiFeP NSs@FeP NDs were labeled with ^{18}O isotopes by potentiostatic reaction for 30 min in KOH solution with $H_2{}^{18}O$. The ^{18}O-labeled catalysts were then rinsed several times with $H_2{}^{16}O$ to remove the remaining $H_2{}^{18}O$. DEMS measurements were carried out by a QAS 100 device (Linglu Instruments, Shanghai). The NiFeP NSs@FeP NDs with ^{18}O-labeling, Pt wire, and Ag/AgCl electrode in saturated KCl solution were used as working, counter, and reference electrode, respectively. The tests were carried out in Ar saturated 1.0 M KOH. CV measurement was performed in KOH solution with $H_2{}^{16}O$ with a scan rate of 5 mV·s^{-1}. Meanwhile, the gas products of different molecular weights were monitored by mass spectroscopy in real time.

2.11 Computational methods

Detailed calculation methods were provided in the Electronic Supplementary Material (ESM).

3 Results and discussion

3.1 Synthesis and characterization of the bimetallic phosphide heterostructures

The rational design of the pre-catalyst is of vital importance for enabling different interfaces to respectively follow the AEM and LOM pathways during *in-situ* dynamic evolution. Here, we choose NiFe-based phosphides as the pre-catalyst due to its advantages that of high catalytic activity and positive role of phosphide in stabilizing the active phase [28]. The synthesis procedures of the NiFeP NSs@FeP NDs bimetallic phosphide heterostructures are illustrated in Fig. 2(a). Ni foam is selected as a conductive support owing to its three-dimensional (3D) macroporous feature and super high electrical conductivity. The bulk $NiFe(OH)_3$ is grown on the Ni foam substrate through the hydrolysis of $Fe(NO_3)_3$ and $Ni(NO_3)_2$ at a constant temperature of 60 °C. As revealed by the SEM images in Fig. S1 in the ESM, the as-prepared $NiFe(OH)_3$ shows bulk structure with large scale size, and grows uniformly around the Ni foam. Afterwards, NiFe LDHs heterostructured FeOOH NDs are obtained via a subsequent alkaline hydrothermal treatment. Interestingly, the huge change in morphology before and after hydrothermal treatment can be attributed to the bottom–up dissolution–recrystallization strategy (detailed synthesis diagram is shown in Fig. S2 in the ESM). Specially, the bulk $NiFe(OH)_3$ dissolves at first with temperature increase and releases a large amount of free Ni^{2+}, Fe^{3+} and OH^- ions in the alkaline solution; then, $Fe(OH)_3$ crystal nucleus preferentially form and grow into $Fe(OH)_3$ NDs owing to its much smaller solubility product constant (K_{sp}) (2.79×10^{-39}) compared to that of $Ni(OH)_2$ (5.92×10^{-15}) [35], resulting in the dramatical decrease of Fe^{3+} concentration to adjoining areas. As Ni^{2+} is eligible to compete with Fe^{3+} in combination with OH^-, the Ni^{2+} and Fe^{3+} ions began to co-precipitate and epitaxically form ultrathin hexagonal bimetallic NiFe LDHs. As shown in Fig. S3 in the ESM, the NiFe LDHs@FeOOH vertically and homogeneously grow on the surface of Ni foam, which interconnect into open architecture with abundant macropores to provide large surface areas and rapid electron transfer. Powder XRD pattern presented in Fig. S4 in the ESM shows a series of characteristic diffraction peaks that matched well with the NiFe LDH (hexagonal, PDF#40-0215) and FeOOH (goethite, PDF#29-0713) [36], suggesting the successful preparation of NiFe LDHs@FeOOH embedded heterostructures and the accuracy of the above growth mechanism. The morphology and structure of NiFe LDHs@FeOOH NDs heterostructure are further characterized by TEM. As shown in Fig. S5(a) in the ESM, TEM image of NiFe LDHs@FeOOH NDs reveals the ultrathin two-dimensional (2D) nanosheet-like characteristics. Closer observation reveals that NiFe LDHs are composed of hexagonal nanosheets with side length of about 150 nm. Moreover, nanoparticles with dimension of several nm are found randomly embedded in the hexagonal nanosheets (Fig. S5(b) in the ESM). HRTEM image

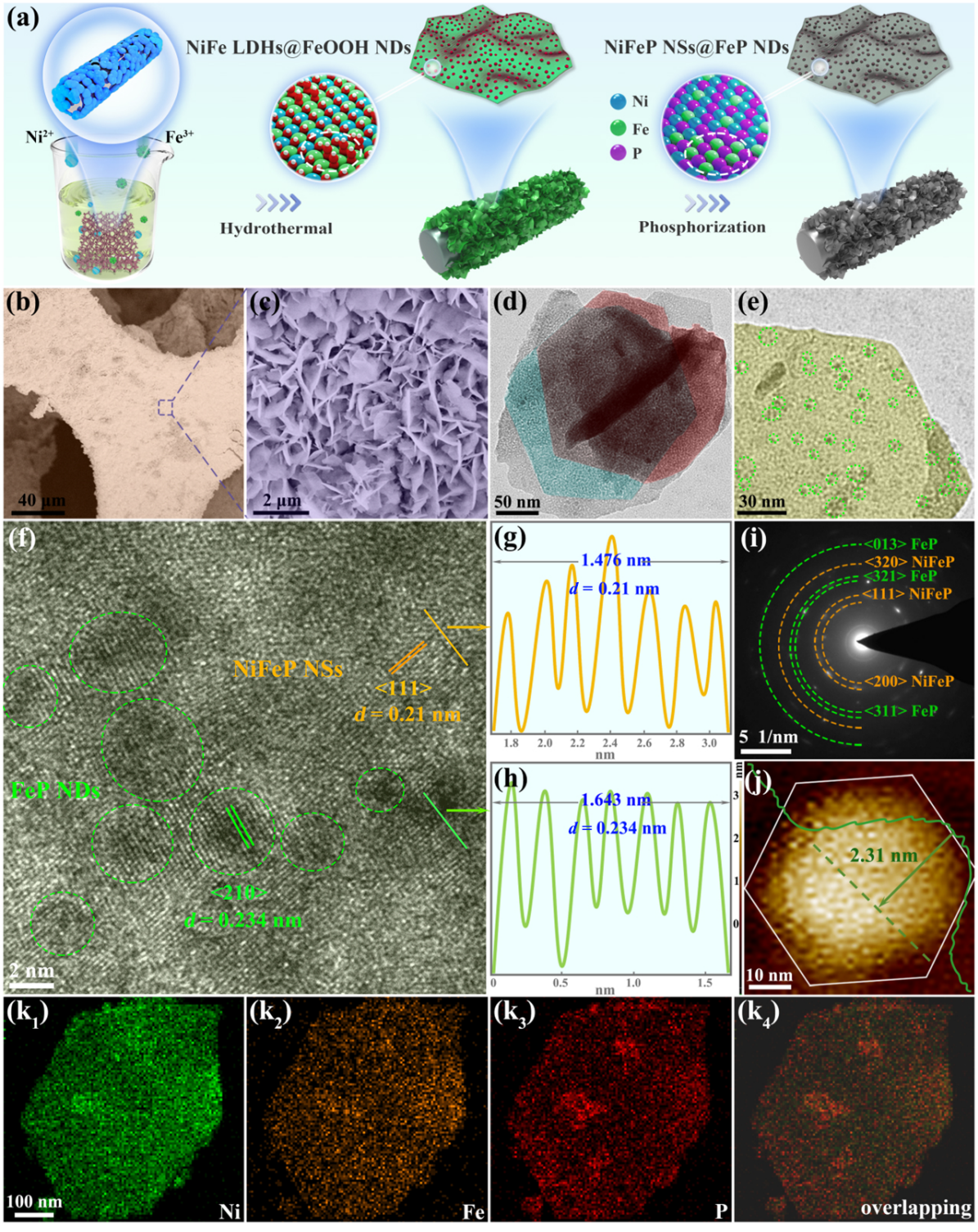

Figure 2 Characterizations of as-prepared NiFeP NSs@FeP NDs electrocatalyst. (a) Schematic illustration of the electrocatalyst preparation. (b) and (c) Typical SEM and ((d) and (e)) TEM images of the heterostructure with different magnifications. (f) HRTEM image. The particles are marked with dotted green lines. (g) Line scan image of NiFeP indicated by the lattice fringe in (f) and (h) line scan image of FeP indicated by the lattice fringe in (f). (i) SAED image. (j) AFM and the corresponding height images. (k_1)–(k_4) EDS elemental mapping images.

taken from the selected coupled area (Fig. S5(c) in the ESM) reveals well-resolved lattice fringes with interplanar distance of 0.26 nm in nanosheet region, 0.24 and 0.19 nm in nanodots region, which respectively indexed to the (012) plane of NiFe LDHs, (111) and (041) planes of FeOOH NDs. Selective area electron diffraction (SAED) pattern of the NiFe LDHs@FeOOH NDs in Fig. S5(d) in the ESM could be indexed into (012), (113), (119) planes for NiFe LDHs, and (111), (221) planes of FeOOH, in accordance with the XRD results. Finally, the NiFe LDHs@FeOOH is further converted into NiFeP NSs@FeP NDs embedded heterostructures (2 mg·cm^{-2})

after low temperature phosphorization under an Ar atmosphere (Fig. S6 in the ESM), and the color of the product transferred from brown to black (Fig. S7 in the ESM). SEM images of NiFeP NSs@FeP NDs displayed in Figs. 2(b) and 2(c) reveal uniformly covered high-density arrays of vertically aligned nanosheet, basically retain the original 2D structure of NiFe LDHs@FeOOH NDs precursor. These 2D nanosheets are arranged neatly on the Ni foam support, staggered into 3D open architecture, which would promote the mass transfer of reactants and products during electrocatalytic process.

The microstructure and crystal texture of the NiFeP NSs@FeP NDs heterostructure could be revealed by TEM. As shown in Fig. 2(d), NiFeP NSs@FeP NDs inherit the hexagonal nanosheet-like morphology and framework well. The transparency of the nanosheets indicates the ultrathin structure of the NiFeP NSs@FeP NDs products. Meanwhile, the hexagonal nanosheets are decorated with nanodots (marked with green dotted circles) as illustrated in Fig. 2(e). The HRTEM image of NiFeP NSs@FeP NDs shown in Fig. 2(f) further reveals the randomly embedded nanodots with diameter of ca. 2–5 nm on the hexagonal nanosheets (marked with green dotted circles). Meanwhile, the clear lattice fringe taken from the nanodots as displayed in Fig. 2(f) also indicates its high crystallization. Besides, the well-resolved lattice fringe with an interplanar spacing of 0.21 nm corresponding to the nanosheet can be assigned to the (111) plane of NiFeP (Fig. 2(g)). The interplanar spacing marked in Fig. 2(h) is 0.234 nm, corresponding to the (210) crystal plane of FeP. The highly dispersed FeP NDs in the ultrathin NiFeP NSs are beneficial to increase the specific surface area of the material and expose more catalytic active sites, thus enhancing the electrocatalytic performance. Moreover, the electronic interactions between NiFeP NSs and FeP NDs are expected to play a crucial role in promoting the electrochemical performance [37]. The SAED diagram (Fig. 2(i)) shows the bright rings composed of discrete spots, corresponding to the (111), (200), and (320) diffraction planes of the NiFeP phase, and the (311), (321), and (013) diffraction planes of the FeP phase. These remarkable structural features are consistent with those of the previously reported nanosheet materials [38]. In contrast, bare $Ni(OH)_2$ and NiP synthesized under the similar experimental conditions (Figs. S8(a) and S8(b) in the ESM) in the absence of $Fe(NO_3)_3{\cdot}9H_2O$ are comprised of irregular nanosheets, while bare $Fe(OH)_3$ and FeP (Figs. S8(c) and S8(d) in the ESM) synthesized without $Ni(NO_3)_2{\cdot}6H_2O$ are composed of nanoparticles. Particularly, no sample is found to cover the surface of Ni foam when Ni and Fe sources are not added (Fig. S9 in the ESM), indicating that Ni atoms on Ni foam not participate in the process of synthesis of the NiFeP NSs@FeP NDs. The formation of vertically NiFeP NSs@FeP NDs hexagonal nanosheets which interconnected into 3D open architecture would be attributed to the competition deposition of $Fe(OH)_3$ and $Ni(OH)_3$ during the hydrolysis process [39]. AFM images in Fig. 2(j) and Fig. S10(a) in the ESM further confirm the hexagonal nanosheet-like structure of NiFeP NSs@FeP NDs with rough surface and the height profile shows the thin thickness of 1.3–2.6 nm (inset in Fig. 2(j) and Fig. S10(b) in the ESM), corresponding to a few atomic layers. The hexagonal nanosheet-like structure with atomic scale thickness endows NiFeP NSs@FeP NDs heterostructure with more exposed active sites, which is expected to improve the electrocatalytic activity of the OER half-cell reaction [40]. The existence of Ni, Fe, and P atoms alongside their homogeneous distribution throughout the whole heterostructure is further proved by the EDS elemental mapping (Figs. 2(k_1)–2(k_4)).

The crystal structure of the NiFeP NSs@FeP NDs heterostructure is further analyzed by XRD, and the resulting patterns are shown in Fig. S11(a) in the ESM. The diffraction pattern of the NiFeP NSs@FeP NDs is nearly identical to that of Ni_2P (PDF#74-1385) and Fe_2P (PDF#51-0943), and the main peaks are found to be located between them, suggesting the formation of NiFeP [37]. In addition to the above diffraction peaks, the remaining minor diffraction peaks can be well assigned to the (120) and (320) planes of FeP (PDF#39-0809). The peaks of FeP NDs are slightly shifted toward higher degree due to the strong interaction between FeP and NiFeP nanosheet in NiFeP NSs@FeP NDs heterostructure. The XPS survey spectrum of NiFeP NSs@FeP NDs (Fig. S11(b) in the ESM) clearly shows Fe, Ni, P, and O elements. The detected O element may be derived from the unavoidably adsorbed oxygen and surface oxidization. The atomic ratio of Ni:Fe:P for the NiFeP NSs@FeP NDs is 55.90:31.92:12.18 (Table S1 in the ESM), in agreement with original ingredient proportion. In the high-resolution Ni 2p spectrum (Fig. S11(c) in the ESM), the peaks of Ni $2p_{3/2}$ at 861.3, 855.9, and 852.1 eV can be attributed to the satellites, Ni^{2+} and Ni–P chemical bonds, respectively [41]. Similarly, the peaks of Ni $2p_{1/2}$ at 879.9 and 873.7 eV represent satellites and Ni^{2+}, respectively [42, 43]. The Fe 2p spectrum (Fig. S11(d) in the ESM) exhibits two major peaks, assigned to Fe $2p_{3/2}$ and Fe $2p_{1/2}$, respectively. The $2p_{3/2}$ peak is composed of bands with peak positions of 704.7, 711.2, and 715.8 eV, which respectively correspond to the Fe–P bond structure, Fe^{3+}, and satellite [44–46]. The 728.3 and 723.9 eV peaks are attributed to the satellite and Fe^{3+}, respectively [47]. The doublet fitted peaks of the P 2p spectrum (Fig. S11(e) in the ESM) at 129.1 and 130.2 eV corresponding to P $2p_{3/2}$ and P $2p_{1/2}$ would be assigned to the P species in transition metal phosphide [48, 49], while the single peak at 133.4 eV can be attributed to the P–O chemical bond [50], indicating the oxidation of phosphorus substances after air exposure. All these results clearly indicate the successful preparation of NiFeP NSs@FeP NDs (as illustrated in Fig. S11(f) in the ESM), which can be used as a pre-catalyst and support the subsequent *in-situ* dynamic activation, as well as facilitating the transformation of different active phases.

3.2 Catalytic activity and stability towards the OER

The electrocatalytic OER performance of as prepared catalysts was tested in 1.0 M KOH electrolyte. These catalysts coated on Ni foam with an area of 1 cm^2 are directly applied as the working electrodes (see the Methods in the ESM for details). Figure 3(a) exhibits the LSV curves of NiFeP NSs@FeP NDs, NiP, and FeP along with commercial IrO_2 (Com-IrO_2) for comparison. Impressively, the NiFeP NSs@FeP NDs heterostructure exhibits super OER performance with a ultralow overpotential of only 197 mV at the current density of 10 $mA{\cdot}cm^{-2}$, which is remarkably lower than that of 288, 240, 280, 297 and 452 mV for bare NiP, FeP, Com-IrO_2, IrO_2/C, and pure Ni foam electrodes (Fig. S12 in the ESM), respectively. Particularly, the OER activity of the NiFeP NSs@FeP NDs electrode shows a trend of initially increasing and then decreasing with the increase of Fe contents (Fig. S13 in the ESM), highlighting a composition-dependent performance. This trend might be attributed to the fact that an optimal Fe facilitates the formation of a uniformly nanosheet-like heterogeneous structure (Fig. 2(d)), while excessive Fe leads to less active Ni/Fe sites on the heterojunction interface due to the formation of coating structure (Fig. S14 in the ESM) [51]. Specially, achieving large current

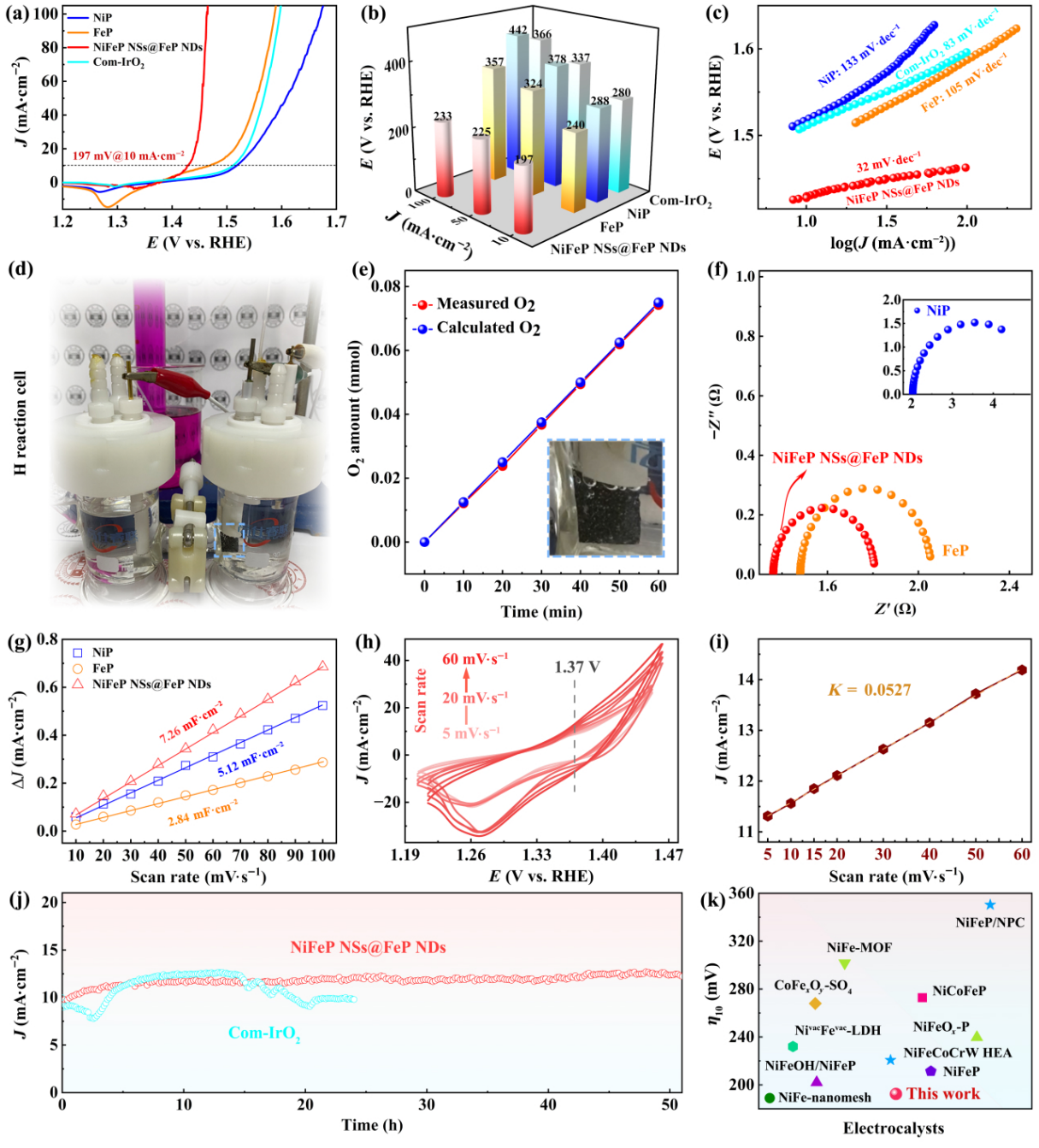

Figure 3 Electrochemical characterization of as-prepared electrocatalysts. (a) LSV curves recorded at a scan rate of 2 mV·s^{-1} in 1.0 M KOH. (b) Overpotential comparison of investigated catalysts at the current densities of 10, 50, and 100 mA·cm^{-2}. (c) Tafel plots of as-prepared catalysts. (d) A fully enclosed H reaction cell with a standard three-electrode system and (e) the amount of O_2 theoretically calculated and experimentally measured versus time for NiFeP NSs@FeP NDs in 1.0 M KOH at a constant current density of 10 mA·cm^{-2}. (f) Nyquist plots and (g) comparison of C_{dl} of various samples according to the CV scans. (h) CV plots at different scan rates of 5, 10, 15, 20, 30, 40, 50, and 60 mV·s^{-1} in 1.0 M KOH and (i) corresponding linear relationship of the oxidation peak currents vs. scan rate at 1.37 V of NiFeP NSs@FeP NDs. (j) Time-dependent OER performance for NiFeP NSs@FeP NDs and Com-IrO_2 at potentials corresponding to current densities of 10 mA·cm^{-2}. (k) Electrocatalytic OER activity for NiFeP NSs@FeP NDs in comparison with other reported catalysts at the current density of 10 mA·cm^{-2}.

densities actuated from small potential is imperative for industrial applications. Therefore, the overpotential at current densities of 10, 50, and 100 mA·cm^{-2} among the as-prepared electrodes is illustrated in Fig. 3(b) for comparison. Of note, only 233 mV overpotential is required for NiFeP NSs@FeP NDs to achieve the large current density of 100 mA·cm^{-2}, indicating its high energy efficiency for catalyzing OER process even at high current density. Moreover, the metallic feature of metallic phosphide and the hybridization of NiFeP NSs and FeP NDs benefit the charge transfer and accelerate the oxidation kinetics with low Tafel slope of 32 mV·dec^{-1}, much smaller than that of bare NiP, FeP, Com-IrO_2, commercial IrO_2/C and pure Ni foam electrodes as depicted in Fig. 3(c) and Fig. S12 in the ESM. Generally, a low Tafel slope indicates a faster reaction kinetics, a lower energy barrier for the electron transfer step or the chemical reaction step [52]. The theoretical value of Tafel slope is directly related to the rate-determining step (RDS) and is believed

to follow the following relationship

$$b = \frac{2.303RT}{(\alpha^{*} + n)F} \quad (1)$$

where b represents the Tafel slope, R is the gas constant, T is the temperature, α is the electron transfer coefficient, and F is the Faraday constant [53–56]. Theoretically, if the elementary RDS transfers one electron (n = 1), then α^{*} = 0.5, and thus the Tafel slope $b \approx 40$ mV·dec^{-1}, which corresponds to the step (II) of the rapid process (i.e., for M-OH* → M-O*). The experimental Tafel slope (32 mV·dec^{-1}) can be reasonably close to the theoretical value of 40 mV·dec^{-1}, considering the inherent experimental factors such as non-ideal nature of the catalyst surface, the double layer effect, and slight temperature fluctuations during the actual operation process. The results indicate that after the heterojunction interface is constructed, the rate-determining step of the OER process is shifted to the step (II). The Faraday efficiency was determined in 1.0 M KOH with a NiFeP NSs@FeP NDs as the working electrode via a drainage method in a fully enclosed H reaction cell with a standard three-electrode system. As shown in Figs. 3(d) and 3(e), the generated O_2 amount matches well with the theoretical value at a constant current density of 10 mA·cm^{-2}, implying a nearly 100% Faradaic efficiency during the OER process.

To elucidate the origin of the reason in the superior OER performance of NiFeP NSs@FeP NDs, EIS measurements were performed at the corresponding overpotential with a current density of 10 mA·cm^{-2}. Generally, a smaller radius of the Nyquist plots corresponds to the faster electron transfer kinetics of the redox reaction and lower charge transfer resistance (R_{ct}). The equivalent circuit at the electrode/electrolyte interface is shown in Fig. S15 in the ESM. As shown in Fig. 3(f), it is clear that NiFeP NSs@FeP NDs have a much smaller Nyquist semicircle diameter than bare FeP and NiP, indicating the lower R_{ct} values of NiFeP NSs@FeP NDs during OER process and the highly efficient electron transfer between FeP NDs and NiFeP NSs [57]. As expected, NiFeP NSs@FeP NDs reveal a smaller impedance (0.4467 Ω) than that of bare NiP (3.037 Ω) and FeP (0.5778 Ω). The lower R_{ct} value is due to the formation of the bimetallic phosphide hetero-interfaces, which can enhance the charge transfer ability, promote the ion transport process, and facilitate effective water splitting, in accordance with above LSV results. Furthermore, electrochemical active surface area (ECSA) is estimated by double-layer capacitance (C_{dl}) deriving from cyclic voltammetry (CV) measurements with different scan rates [58]. As shown in Fig. S16 in the ESM, in the absence of a redox process, CV measurements are performed in the potential range of the non-faradaic zone at different scan rates from 20 to 200 mV·s^{-1}. The calculated C_{dl} of NiFeP NSs@FeP NDs heterostructure is 7.26 mF·cm^{-2}, higher than NiP (5.12 mF·cm^{-2}) and FeP (2.84 mF·cm^{-2}) (Fig. 3(g)). ECSA-corrected LSV curves in Fig. S17 in the ESM further confirm that NiFeP NSs@FeP NDs exhibit the highest intrinsic activity, consistent with the results of the un-normalized results in Fig. 3(a). Moreover, as determined by N_2 sorption measurement (Fig. S18 and Table S2 in the ESM), the NiFeP NSs@FeP NDs diaplay a higher BET specific surface area of 83.48 m^2·g^{-1} compared to that of NiP (17.17 m^2·g^{-1}) and FeP (31.55 m^2·g^{-1}). Furthermore, the volume adsorbed and BET values are both higher than those of the non-phosphated samples (Fig. S19 and Table S3 in the ESM), which might be attributed to the thermal polymerization of the catalyst caused by high-temperature phosphating, which in turn led to a reduction in the size of the catalyst (as demonstrated by SEM images in Fig. S8 in the ESM). The higher C_{dl} and BET values of NiFeP NSs@FeP NDs would be derived from its 3D open architecture comprised of ultrathin nanosheets, representing large ECSA and more active sites exposure for reaction, which favors the superior OER catalytic activity. Meanwhile, we calculated the turnover frequency (TOF) value using the reported methods to investigate the intrinsic catalytic activity [59]. The concentration of active sites in the catalysts (mol·cm^{-2}) is estimated by CV sweeps for the redox reaction at different scan rates (Fig. 3(h)). It should be noted here that the redox active sites are not all catalytically active, the calculated TOF would be the lower limit for the catalyst. The linear relationship of the oxidation peak currents vs. scan rate at 1.37 V in the CVs was determined to be k = 0.0527 (Fig. 3(i)). Accordingly, it can be calculated that the average TOF value of the NiFeP NSs@FeP NDs catalyst is 0.05 s^{-1} at the overpotential of 197 mV. Aside from the superior OER activity, the catalytic stability is another key parameter for practical application. As shown in Fig. 3(j) and Fig. S20 in the ESM, the OER activity of NiFeP NSs@FeP NDs displayed no obvious decay during long-term chronoamperometric (i–t) and chronopotentiometry (E–t) tests at the overpotential of 197 mV and current density of 50 mA·cm^{-2}, respectively. On the contrary, the commercial IrO_2 electrode showed poor stability, which confirms the potential application value of NiFeP NSs@FeP NDs. Moreover, we operated the long-term stability of the NiFeP NSs@FeP NDs and commercial IrO_2 electrodes under a high current density of 500 mA·cm^{-2} to evaluate the potential practical applications. In sharp contrast to commercial IrO_2, NiFeP NSs@FeP NDs maintain stable operation for 200 h at 500 mA·cm^{-2} with only slight attenuation (Fig. S21 in the ESM), fully illustrating the remarkable OER catalytic stability. In addition, the LSV polarization curve of the same NiFeP NSs@FeP NDs electrode after 3000 CV cycles is also recorded (Fig. S22 in the ESM). It could be found that NiFeP NSs@FeP NDs heterostructure displays almost the same LSV curve as initial curve and maintains the low overpotential. Particularly, the overpotential of NiFeP NSs@FeP NDs compared with the reported transition metal-based catalysts demonstrates the superior OER performance in 1.0 M KOH (Fig. 3(k) and Table S4 in the ESM).

3.3 *In-situ* and *ex-situ* characterization of the active phases

One of the currently widely accepted viewpoints is that the surface active phase of transition metal phosphides reconfigures into hydroxides or (oxy)hydroxides in alkaline medium, serving as real active phases that are beneficial for the OER. Considering the outstanding performance of the prepared bimetallic phosphide heterostructure, it can be inferred that as the overpotential increases during the OER process, a dynamic activation transformation of active phases must occur on the surface of the catalyst, and the metal phosphides also played an indispensable and beneficial role. Nevertheless, our experimental results show that the overpotential of the precursor electrode NiFe LDHs@FeOOH NDs before phosphating requires a overpotential of 241 mV to reach the current density of 10 mA·cm^{-2} (Fig. S23 in the ESM), dramatically worse than that of the phosphated NiFeP NSs@FeP NDs electrode (197 mV), as well as the Tafel slope. Therefore, in order to gain a deeper understanding of the dynamic activation transformation process of the real active phase and the OER reaction mechanism, we conducted systematic *in-situ* and *ex-situ* characterizations.

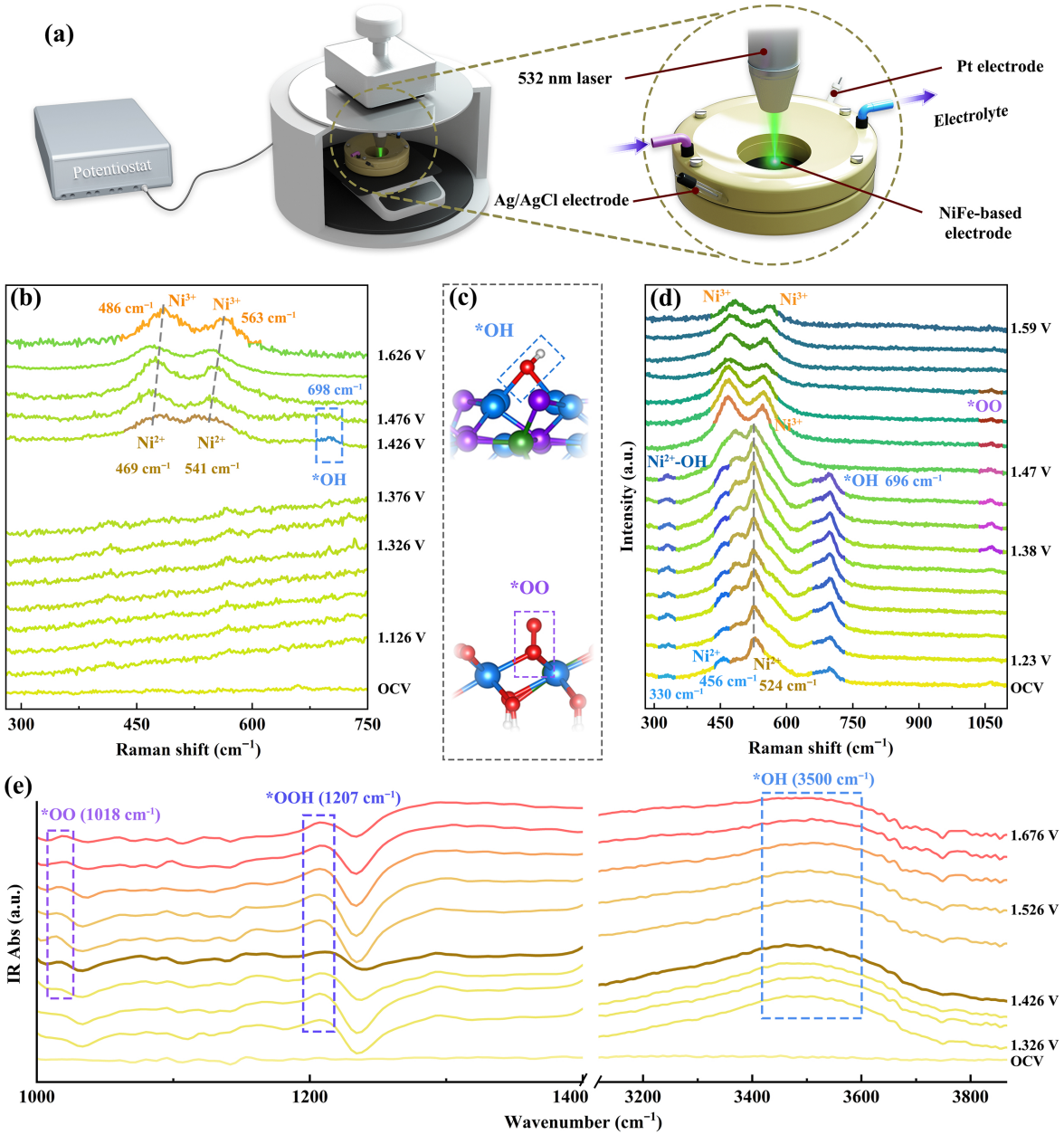

Figure 4 *In-situ* structural characterization of as-prepared electrocatalysts. (a) Schematic illustration of the *in-situ*/*operando* Raman spectroscopy setup. (b) *In-situ* Raman spectra of OER on NiFeP NSs@FeP NDs using a 532 nm laser. (c) The structures of *OH and *OO intermediate species resulting from DFT simulations. (d) *In-situ* Raman spectra of OER on NiFeP NSs@FeP NDs that have undergone long-term OER reactions using a 532 nm laser. (e) *In-situ* FTIR spectra of OER on NiFeP NSs@FeP NDs. All potentials were normalized against reversible hydrogen electrode.

Firstly, *in-situ* Raman spectroscopy measurements were employed to unveil the dynamic changes of our catalysts in the active intermediates during the OER process, the reaction cell is shown in Fig. 4(a). Initially, no significant change was observed in the potential from OCV to 1.326 V vs. RHE (Fig. 4(b)), which indicates that the surface of the catalyst has not yet undergone structural evolution, which means it is still in the pre-oxidation stage and retains the phosphide properties. As the potential increases to 1.326–1.626 V (vs. RHE), a series of characteristic peaks with dynamic changes emerged. Specifically, the peak intensity at 698 cm^{-1} initially increased, then gradually decreased, and finally disappeared. Compared our *in-situ* Raman spectroscopy results with the above reported work, the Raman peak at 698 cm^{-1} would be ascribed to the adsorbed *OH intermediate on catalyst [19, 28, 60, 61]. Moreover, two additional Raman signals of E_g (469 cm^{-1}) and A_{1g} (541 cm^{-1}) that respectively attributed to the oxidation of Ni^{2+} on the spectra within the potentials of 1.426–1.476 V (vs. RHE) were also observed [62, 63], which suggests that dynamic surface reconfiguration occurs on the catalyst surface and leads to the formation of hydroxides. However, once the potential surpasses 1.476 V (vs. RHE), the signal from *OH has disappeared, and the $Ni^{\delta+}$ vibration peak has gradually shifted to a higher wavenumber range (E_g: 486 cm^{-1} and A_{1g}: 563 cm^{-1}), indicating the dynamic surface reconstruction into the higher valence Ni^{3+} species [64]. That is to say, during this process, all the Ni-OH on the catalyst surface undergoes a complete deep reformation into Ni-OOH.

Moreover, a series of vibration peaks located around 1150 cm^{-1} are attached to *OOH intermediates (Fig. S24 in the ESM) formed during the OER under AEM pathway [65, 66]. Meanwhile, the obvious vibration peak at 1063 cm^{-1} also appeared in the potential interval 1.426–1.626 V (vs. RHE, Fig. 4(b)), and associated with superoxidic species (*OO) resulting from the deprotonation process [19], which serve as crucial intermediates in the LOM pathway and promoting subsequent O–O coupling during the OER. These observations indicate that with the dynamic transformation of the surface-active phase, the AEM-LOM synergistic pathway is activated, effectively improving the OER performance.

In order to further verify the above results, NiFeP NSs@FeP NDs electrode that had been operated for 50 h at a current density of 10 $mA{\cdot}cm^{-2}$ was also conducted by *in-situ* Raman spectroscopy. As shown in Fig. 4(c), it was identified that Ni^{2+} and *OH species were present on the surface of the catalyst after long-term OER operation, and remained unchanged until a potential of 1.47 V (vs. RHE), consistent with the results reported in previous studies [67–69]. On the contrary, Ni-OH disappears and the surface-active phase transforms into the NiOOH species when the potential exceeds 1.47 V (vs. RHE). Moreover, it was observed that the two *OH and *OO species were only involved in the OER reaction within the potential range of 1.38–1.47 V vs. RHE electrode (i.e., 150–240 mV when the standard potential is subtracted by 1.23 V). These results indicate that under the operating conditions of our electrolyzer (197 mV@10 $mA{\cdot}cm^{-2}$), the active phases on the catalyst surface are not in the highly oxidized state of N^{3+}, but rather N^{2+} species (i.e., hydroxides). *In-situ* FTIR technology was further employed to unveil the oxygen intermediate species generated on the NiFeP NSs@FeP NDs during OER process. As shown in Fig. 4(d), three distinct absorption peaks can be observed near 1018, 1210, and 3500 cm^{-1} with the elevated potentials, indicating the production of oxygenated intermediates. The peak located at 1210 and 3500 cm^{-1} can be attributed to the *OOH and *OH intermediates formed during the AEM pathway [66, 70]. Specially, the peak at about 1018 cm^{-1} is attached to the *OO [65, 71], further suggesting the involvement of LOM pathway on that catalyst. It should be noted that no characteristic vibration bands related to phosphorus P^{n+} species were found in the *in-situ* spectrum, indicating that phosphate formation was not involved in the dynamic reconfiguration process of the catalyst during the OER process [72–74].

XPS was also performed after long-term OER test to identify the changes in atomic valence. As represented in Fig. S25(a) in the ESM, the Ni–P peak (852.1 eV) in the high-resolution Ni 2p XPS spectrum of the NiFeP NSs@FeP NDs is significantly weakened and shifts to the higher binding energy (~ 0.3 eV), implying the surface oxidation of Ni–P [75, 76]. The similar tendency can also be seen in the Fe 2p spectra (Fig. S25(b) in the ESM). On the contrary, the high-resolution P 2p XPS spectrum (Fig. S25(c) in the ESM) shows a negatively shifted binding energy, and the P $2p_{3/2}$ and P $2p_{1/2}$ components are still maintained, which confirms the coexist metal phosphides and hydroxide active phases on the surface of the catalyst during the OER process. Furthermore, we conducted SEM and TEM analyses on the electrodes after long-term OER to investigate the structural evolution on their surfaces. Obviously, SEM images in Figs. S26(a) and S26(b) in the ESM still show the same interlaced nanosheet open structure as before the OER test (Fig. 2(c)). Moreover, TEM and HRTEM images in Figs. S26(c) and S26(d) in the ESM demonstrate the catalyst still maintains an ultrathin nanosheet structure with a large number of particles embedded on the surface, except for the additional lamellar structure (wathet label) covered on the nanosheet, suggesting that (oxy)hydroxides might be *in-situ* generated during OER test. As shown in Fig. S26(e) in the ESM, the lattice fringes matched to the (012) crystal plane of NiFe LDH (PDF#40-0215), as well as NiFeP NSs and FeP NDs were found, suggesting that both the phosphide and hydroxide active phases remain on the surface of the catalyst. However, no lattice fringes related to Ni-based (oxy)hydroxides (PDF#06-0075) were observed, which is consistent with the results of *in-situ* Raman spectroscopy. ICP-OES also confirmed the presence of phosphides after the long-term OER test (Table S5 in the ESM). More accurate HRTEM image (Fig. S26(g) in the ESM) in the selected boundary area in Fig. S26(f) in the ESM and SAED image (Fig. S26(h) in the ESM) further confirm this conclusions.

Based on the above *in-situ* and *ex-situ* analysis results, the dynamic structural evolution process of the active phase on the surface of the NiFeP NSs@FeP NDs catalyst may be as shown in Fig. S26(i) in the ESM. Initially, the NiFeP NSs@FeP NDs electrode is immersed in an alkaline electrolyte. As the applied potential gradually increases, hydroxide ions adsorb onto the surface of the catalyst and form an incomplete coating of hydroxides on the surface of the phosphides with the extracted metal ions. When the applied potential exceeds the critical point of 1.47 V (vs. RHE), the Ni^{2+} species on the surface are deeply oxidized to Ni^{3+} species, forming (oxy)hydroxides. The interesting aspect lies in the fact that under this dynamic activation condition, the phosphide species are not completely covered by the surface oxidized species, which allows for the possibility that different components can respectively follow the AEM and LOM pathways. The above conclusions will be further elaborated in the subsequent theoretical calculations, oxygen isotope labeling, and DEMS.

3.4 Insight into AEM-LOM synergistic mechanism

To further elucidate the AEM-LOM synergistic mechanism of OER, we conducted ^{18}O isotope labeling and DEMS measurements to directly verify whether both adsorbed oxygen and lattice oxygen species exist simultaneously during the OER process. Figure 5(a) shows the DEMS apparatus, and the gas chromatography method was used to analyze the $^{36}O_2$ (n = 2, 4, 6) species that were generated through evolution. The catalyst is first labeled with the ^{18}O isotope through CV cycle in a $H_2{}^{18}O$-containing alkaline electrolyte. After thoroughly cleaning the ^{18}O-labeled catalyst using $H_2{}^{16}O$ deionized water, the anodic oxygen evolution reaction was carried out in the $H_2{}^{16}O$ electrolyte with pure Ar as the carrier gas (see the Methods in the ESM for details). Generally, the composition of the gaseous O_2 products can be used to distinguish whether the OER follows the AEM or the LOM pathway (Fig. 5(b)) [77]. The DEMS results (Fig. 5(c)) of NiFeP NSs@FeP NDs without ^{18}O labeling reveal $^{16}O^{16}O$ (m/z = 32) signals, while almost no $^{16}O^{18}O$ and $^{18}O^{18}O$ are detected. Whereas, the ^{18}O-labeled catalysts exhibit significant $^{16}O^{16}O$ and $^{18}O^{16}O$ (m/z = 34) signals (Fig. 5(d)), indicating that both adsorbed oxygen and lattice oxygen are involved in the oxygen release process and the detected ^{18}O originates from the labeled lattice oxygen in the catalyst, consistent with the previous studies [16, 21]. It is well known that catalysts following the LOM pathway can effectively enhance the intrinsic activity of OER. However, if the lattice O loss and replenishment cannot reach a dynamic equilibrium, the O vacancies generated by lattice oxygen escape will weaken the bonding between adjacent metal atoms, thereby leading

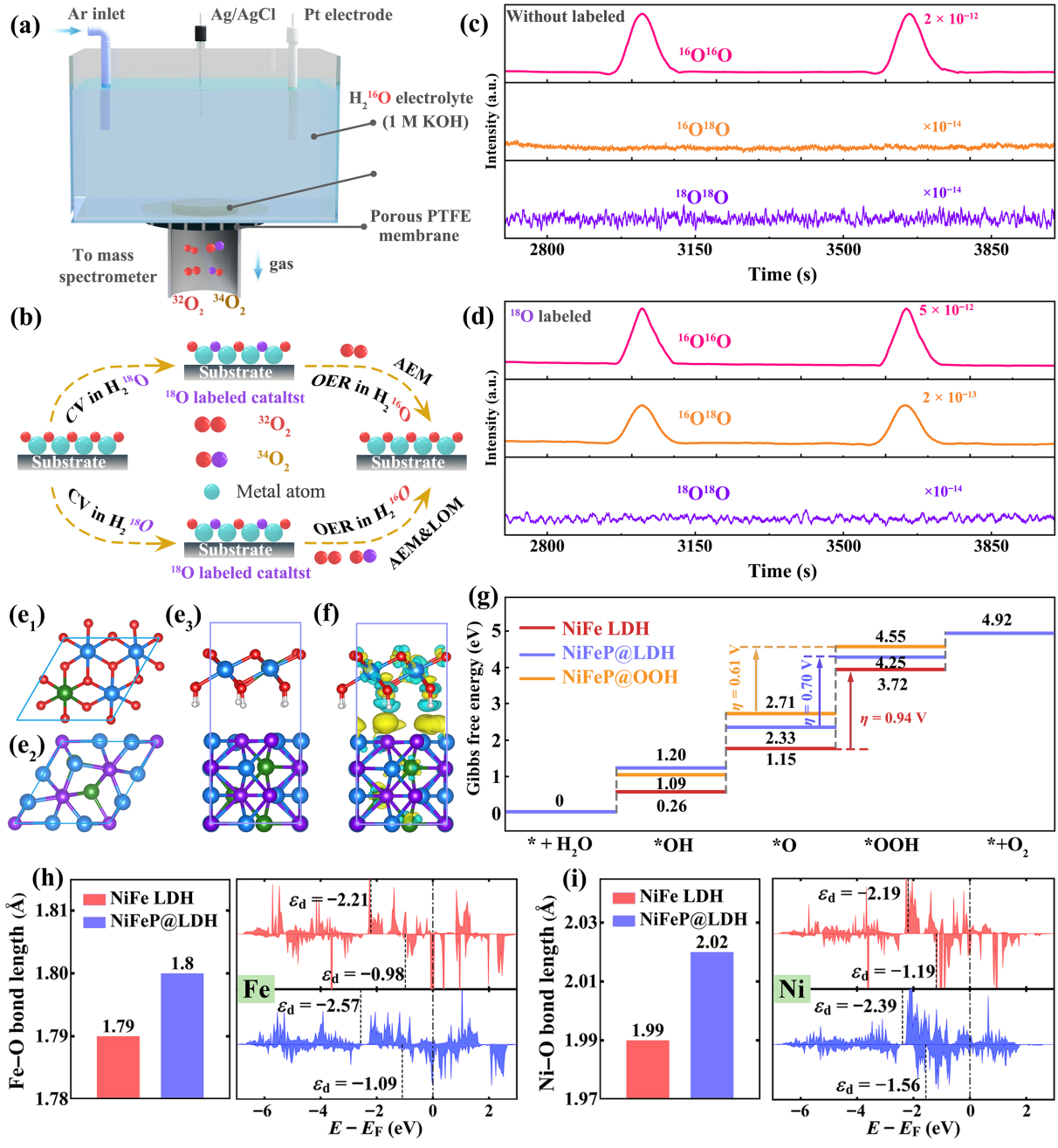

Figure 5 AEM-LOM synergistic mechanism of OER catalysis analysis. (a) Schematic illustration of the DEMS setup and (b) corresponding ^{18}O substitution experiment involving the AEM and LOM pathways. DEMS signals of $^{16}O^{16}O$ (^{32}O), $^{16}O^{18}O$ (^{34}O), and $^{18}O^{18}O$ (^{36}O) over time for NiFeP NSs@FeP NDs electrocatalyst (c) without ^{18}O label and (d) with ^{18}O label. Optimized structures of (e_1) NiFe LDH, (e_2) NiFeP, (e_3) NiFeP and NiFe LDH interface. (f) 3D electron density difference between NiFe LDH and NiFeP, the yellow (blue) region indicates the electron accumulation (depletion). (g) The calculated Gibbs free energy diagram for OER of pure NiFe LDH, NiFeP@NiFe LDH (NiFeP@LDH), and NiFeP@NiFeOOH (abbreviated as NiFeP@OOH) at U = 0 V. The bond length between O atom and metal atom (left panel) and the calculated d-orbital-PDOS (right panel) for pure NiFe LDH (red) and NiFeP@LDH (blue) at (h) Fe site and (i) Ni site.

to the dissolution of Ni active sites and structural disorder. Obviously, EPR curves of the NiFeP NSs@FeP NDs shown in Fig. S27 in the ESM confirm that the oxygen vacancy concentration exhibits a dynamic filling relationship as the applied voltage increases and decreases. Moreover, the signal intensity of $^{16}O^{16}O$ in the ^{18}O-labeled NiFeP NSs@FeP NDs is higher than that of $^{18}O^{16}O$ (Fig. 5(d)), implying the reaction mainly involved AEM pathway, thereby resulting in better durability in the experiment.

DFT calculations were further conducted to gain a deeper understanding of the AEM-LOM synergistic mechanism induced by the evolution of active phases. The optimized structures of FeP(001), NiFeP(001), and NiFeP@FeP heterostructure are shown in Figs. S28(a)–S28(c) in the ESM with intermediates of OER process adsorbing on different active sites (AEM pathway). Under U = 1.23 V, the reaction steps (I) and (II) on both FeP(001) and NiFeP(001) surfaces occur spontaneously with significant drops in free energy, and the reaction step (III) is revealed as a RDS with the overpotential of 1.29 and 1.79 V, respectively, on P site of FeP(001) surface and Ni site of NiFeP(001) surface (Fig. S28(d) and Table S6 in the ESM). However, the adsorption of *OOH intermediate on P

site of NiFeP(001) surface is unstable and it spontaneously dissociates to *O and *OH adsorbates, which implies that the formation of *OO intermediate is the RDS with the overpotential of 3.58 V. Similarly, the RDS is step (IV) for the P site at NiFeP@FeP interface, in which the adsorbed *OOH is unstable and the corresponding overpotential is 3.91 V, suggesting that the sluggish OER process is unlikely to happen at interfacial P site. Miraculously, the step (II) (formation of *O from *OH) on the interfacial Ni site with unique local coordination environments, presents the highest free energy change, i.e., it is the RDS with a very low overpotential of 0.55 V. Therefore, Ni atoms at dense interfaces as catalytically active sites alters the RDS from step (III) (*O to *OOH) in NiFeP to step (II) (*OH to *O) in the NiFeP@FeP heterostructure, consistent with the conclusion derived based on the Tafel slope. As a result, *OOH is easier to form on NiFeP@FeP heterostructure, which will facilitate the production of O_2. These results demonstrate that the formation of NiFeP@FeP interface is beneficial to decrease Gibbs free energies and enhance the activity through AEM pathway during OER process. Moreover, the d-orbital-projected density of states (PDOS) and corresponding d-band center (ε_d) of Ni site at NiFeP and NiFeP@FeP interface are investigated and displayed in Fig. S28(e) in the ESM. The calculated ε_d of Ni site of NiFeP is −1.43 eV and that of interfacial Ni site is −1.51 and −1.53 eV for spin-up and spin-down d-states respectively, indicating a down-shift of ε_d when the NiFeP@FeP interface is formed. From the perspective of the d-band center theory, the decrease of ε_d energy level enhances the electron filling of antibonding states, thus reducing the bond strength between surface and intermediates [78]. Therefore, the interfacial Ni site has significantly weakened adsorption of the OER intermediates relative to the Ni site of NiFeP. More importantly, G_{*O} is weakened more than G_{*OH}, which increase the free energy of *O adsorbate effectively, changing the RDS to step (II) and lowering the overpotential to 0.55 V (Fig. S29 in the ESM). Moreover, as illustrated in Fig. S28(f) in the ESM, the formation of NiFeP@FeP interface increases the DOS of Ni site near the Fermi level compared to the NiFeP, resulting in an increase in electroconductivity. These results suggest that the interfacial Ni atoms with unique local coordination environments are predominately responsible for the experimentally observed enhancement in the specific activity of NiFeP@FeP heterostructure compared to NiFeP, which would motivate to optimize the properties of Ni-Fe phosphide systems. Furthermore, the electron density difference of bare NiFeP@FeP interface and the interface with an oxygen atom adsorbed is studied to analyze the charge redistribution effect at the interface. The amounts of electron transfer at the bare NiFeP@FeP interface can be visualized by the 3D electron density difference in the Fig. S30(a) in the ESM, where the red and blue region represents the electron accumulation and depletion, respectively. The red region is mainly distributed around the P atom at the interface and the blue region mainly around Ni and Fe atom, indicating that the formation of NiFeP@FeP interface facilitates the charge transfer between NiFeP and FeP. Moreover, when the oxygen atom adsorbed on the interface (Fig. S30(b) in the ESM), the Ni atom serves as an electron donor whereas the P atom and O atom as the electron acceptor, thus changing the free energy of *O adsorbate effectively [79].

The results from TEM, *in-situ* Raman spectroscopy, and DEMS experiments demonstrate that the interface of NiFeP@NiFe LDH (NiFeP@LDH) can effectively enhance the activity of the OER through the LOM pathway. The optimized structures of NiFe LDH, NiFeP, and NiFeP@LDH heterostructure are shown in Figs. 5(e_1)–5(e_3). The bonding energy E_b is calculated by the following equation: $E_b = E_{total} - E_{NiFe\text{-}LDH} - E_{NiFeP}$. The short layer distance of 2.03 Å and the negative bonding energy of −1.93 eV indicate that NiFe LDH can be stably present on the NiFeP surface through vdW interaction. In addition, the apparent charge transfer between NiFeP and NiFe LDH further confirms the stable VdW interaction, as indicated in the 3D electron density difference (Fig. 5(f)). Moreover, except for stably supporting NiFe LDH, the interface interaction can significantly improve the catalytic activity of NiFeP@LDH from the Gibbs free energy landscape (Fig. 5(g)), which lowers the theoretical OER overpotential from 0.94 to 0.70 V compared to NiFe LDH (pure LDH). Moreover, we also utilized DFT calculations to investigate the influence of the formation of the NiFeP@NiFeOOH (NiFeP@OOH) interface structure under high voltage on the kinetics of oxygen evolution reaction. The optimized structure of the NiFeP@OOH heterostructure is shown in Fig. S31 in the ESM. Obviously, as shown in Fig. 5(g), the formation of the NiFeP@OOH interface further reduces the theoretical OER overpotential to 0.61 V. The above results indicate that at higher voltages, the dynamic reconfiguration of the catalyst surface to form (oxy)hydroxides, as a highly active phase, can significantly enhance the performance of the OER. Due to the enrichment of O atoms, the OER cycle is always produced by LOM pathway. On the surface of NiFe LDH, the lattice oxygen participates in the OER cycle as part of intermediate and leads to a dual-metal-site LOM pathway, consistent with the results reported in previous studies [15, 80]. What is fantastic thing is that the interface interaction weakens the bond strength between metal and O atoms because of higher free energy (ΔG = 0.94, 1.18, and 0.53 eV) for all intermediates (*OH, *O, and *OOH) compared to pure NiFe LDH. Besides, the Fe–O (Ni–O) bond length and d-orbital-PDOS for Fe (Ni) site are calculated in Figs. 5(h) and 5(i). After forming interface, both Fe–O and Ni–O bonds become longer verifying the weakened bond interaction. More importantly, from the PDOS calculation, the ε_d reduced from −2.21 eV (−0.98 eV) to −2.57 eV (−1.09 eV) for spin-up (spin-down) channel at Fe site, and reduced from −2.19 eV (−1.19 eV) to −2.39 eV (−1.56 eV) for spin-up (spin-down) channel at Ni site, indicating that both Fe and Ni sites will weaken the adsorption of O atom according to the d-band center theory. The reason of above phenomenon can be attributed to that the charge transfer from NiFe LDH layer to NiFeP (Fig. 5(f)) leads to the electron depletion at both O and metal sites in NiFe LDH layer. And this electron depletion rooting in interface interaction can further reduce bond interaction and reduce d-band center of metal sites promoting the activation and desorption of lattice oxygen, which can significantly improve OER performance through LOM cycle. These theoretical calculations are in excellent agreement with the experimental results, further confirming the the idea that the *in-situ* dynamic activation of the active phases effectively combines the advantages of the AEM and LOM pathways, effectively reducing the OER energy barrier and thereby promoting the OER performance.

4 Conclusions

In summary, we have reasonably designed a bimetallic phosphide heterojunction as a pre-catalyst, which facilitates the dynamic transformation of its surface into coexisting phosphides and hydroxides as the active phases during OER. The ^{18}O isotope labeling combined with DEMS and *in-situ* Raman spectroscopy

measurements confirmed that anode activation could promote the release of adsorbed oxygen, and lattice oxygen during the oxygen release process, thereby facilitating the effective synergy of the AEM-LOM pathway. Density functional theory calculations reveal the key roles of the unique interface environments of active phases in improving OER activity. Ni atoms as active sites at dense phosphide heterointerfaces reduce the electrochemical reaction barrier via tuning the formation processes of O* and OOH* under the AEM pathway. Meanwhile the interface interaction in NiFeP-NiFe LDH weakens the metal-bond, as well as lowers the d-band center of metal sites, promoting the activation of O–O coupling and desorption of lattice oxygen under the LOM pathway. As a result, the activated catalyst integrates the advantages of the each pathways of AEM and LOM, and possesses high intrinsic OER catalytic activity and stability. This work provides inspiration for designing highly active and cost-effective catalysts and new insights for further understanding of the OER mechanism of transition metal phosphides.

Electronic Supplementary Material: Supplementary material (detailed calculation methods, additional XRD, SEM, TEM/HRTEM, AFM, XPS, nitrogen adsorption–desorption isotherms, *in-situ* Raman spectra, DFT data of control samples and catalysts, more electrocatalytic tests data (CV plots, LSV curves, ECSA, chronopotentiometry (*E*–*t*) tests), and comparison Tables of OER property (PDF)) is available in the online version of this article at https://doi.org/10.26599/NR.2026.94908466.

Data availability

All data needed to support the conclusions in the paper are presented in the manuscript and the Electronic Supplementary Material. Additional data related to this paper may be requested from the corresponding author upon request.

Acknowledgements

The authors are grateful to the National Natural Science Foundation of China (Nos. 52401287 and 52571246) and the Doctoral Research Start-up Fund Project of Shangqiu Normal University (No. SQNUQDF2402). We would also like to appreciate the computation platform of National Supper-Computer Center in Changsha.

Declaration of competing interests

The authors declare that they have no known competing financial interests or personal relationships that could have appeared to influence the work reported in this paper.

Author contribution statement

B. L.: Data curation, project administration, validation, writing manuscript, experimental design, funding acquisition. Y.-H. W.: Data curation, validation, investigation. T. H. and L. L.: Validation, investigation. Q. F. and J. H. S.: Investigation. G.-F. H.: Writing – review & editing, funding acquisition. W. Y. H.: Validation, investigation. W.-Q. H.: Project administration, funding acquisition, writing – review & editing. All the authors have approved the final manuscript.

Use of AI statement

None.

References

[1] Johnson, N.; Liebreich, M.; Kammen, D. M.; Ekins, P.; McKenna, R.; Staffell, I. Realistic roles for hydrogen in the future energy transition. *Nat. Rev. Clean Technol.* **2025**, *1*, 351–371.

[2] Li, B.; Peng, W.; Zhang, J.; Lian, J. C.; Huang, T.; Cheng, N.; Luo, Z. Y.; Huang, W. Q.; Hu, W. Y.; Pan, A. L. et al. High-throughput one-photon excitation pathway in 0D/3D heterojunctions for visible-light driven hydrogen evolution. *Adv. Funct. Mater.* **2021**, *31*, 2100816.

[3] Wan, C. Z.; Zhang, Z. S.; Dong, J. C.; Xu, M. J.; Pu, H. T.; Baumann, D.; Lin, Z. Y.; Wang, S. B.; Huang, J.; Shah, A. H. et al. Amorphous nickel hydroxide shell tailors local chemical environment on platinum surface for alkaline hydrogen evolution reaction. *Nat. Mater.* **2023**, *22*, 1022–1029.

[4] Chao, T. T.; Xie, W. B.; Hu, Y. M.; Yu, G.; Zhao, T. H.; Chen, C.; Zhang, Z. D.; Hong, X.; Jin, H. L.; Wang, D. S. et al. Reversible hydrogen spillover at the atomic interface for efficient alkaline hydrogen evolution. *Energy Environ. Sci.* **2024**, *17*, 1397–1406.

[5] Li, Z. B.; Wu, R. Y.; Duan, D. B.; Liu, X. J.; Li, R.; Wang, J.; Chen, H. W.; Chen, S. W.; Wu, Y.; Wang, H. et al. Empowering multicomponent alloys with unique nanostructure for exceptional oxygen evolution performance through self-replenishment. *Joule* **2024**, *8*, 2920–2937.

[6] Israr, M.; Humayun, M.; Zhang, J. Q.; Shah, K.; Tan, X.; Chen, C.; Li, Y. D. Ir single atoms on NiFeZn-LDH matrix for exceptional oxygen evolution reaction. *Nano Res.* **2024**, *17*, 7039–7044.

[7] Li, C. Y.; Wang, Z. J.; Liu, M. D.; Wang, E. Z.; Wang, B. L.; Xu, L. L.; Jiang, K. L.; Fan, S. S.; Sun, Y. H.; Li, J. et al. Ultrafast self-heating synthesis of robust heterogeneous nanocarbides for high current density hydrogen evolution reaction. *Nat. Commun.* **2022**, *13*, 3338.

[8] Zhang, J. H.; Fu, X. B.; Kwon, S.; Chen, K. F.; Liu, X. Z.; Yang, J.; Sun, H. R.; Wang, Y. C.; Uchiyama, T.; Uchimoto, Y. et al. Tantalum-stabilized ruthenium oxide electrocatalysts for industrial water electrolysis. *Science* **2025**, *387*, 48–55.

[9] Yu, Y.; Zhou, W.; Zhou, X. H.; Yuan, J. S.; Zhang, X. W.; Meng, X. X.; Sun, F.; Gao, J. H.; Zhao, G. B. Taking advantage of activation potential coincidence to unlock stable direct seawater splitting. *Adv. Funct. Mater.* **2025**, *35*, 2419871.

[10] Magnier, L.; Cossard, G.; Martin, V.; Pascal, C.; Roche, V.; Sibert, E.; Shchedrina, I.; Bousquet, R.; Parry, V.; Chatenet, M. Fe-Ni-based alloys as highly active and low-cost oxygen evolution reaction catalyst in alkaline media. *Nat. Mater.* **2024**, *23*, 252–261.

[11] Zhao, J.; Guo, Y.; Zhang, Z. Q.; Zhang, X. L.; Ji, Q. Q.; Zhang, H.; Song, Z. Q.; Liu, D. Q.; Zeng, J. R.; Chuang, C. et al. Out-of-plane coordination of iridium single atoms with organic molecules and cobalt-iron hydroxides to boost oxygen evolution reaction. *Nat. Nanotechnol.* **2025**, *20*, 57–66.

[12] Xu, H. M.; Yue, K. H.; Song, L. J.; Zhang, H. C.; Zhu, H. R.; Zhang, Z. J.; Li, G. R. The asymmetrical Fe−O−Se bonds in $Fe_2O(SeO_3)_2$ boosting bifunctional oxygen electrocatalytic performance for zinc-air battery. *Angew. Chem., Int. Ed.* **2024**, *63*, e202412025.

[13] Wang, X. P.; Xi, S. B.; Huang, P. R.; Du, Y. H.; Zhong, H. Y.; Wang, Q.; Borgna, A.; Zhang, Y. W.; Wang, Z. B.; Wang, H. et al. Pivotal role of reversible NiO_6 geometric conversion in oxygen evolution. *Nature* **2022**, *611*, 702–708.

[14] Mattioli, G.; Guidoni, L. Multiple reaction pathways for oxygen evolution as a key factor for the catalytic activity of nickel-iron (oxy)hydroxides. *J. Am. Chem. Soc.* **2025**, *147*, 6450–6463.

[15] Yang, X. Y.; Chen, Z. D.; Zhang, G. X.; Sun, Y. P.; Lu, J. B.; Lin, H. P.; Fan, X. Advances in oxygen evolution reaction electrocatalysts via direct oxygen-oxygen coupling pathway: Recent progress, challenges, and perspectives. *Nano Res.* **2026**, *19*, 94907881.

[16] Luo, X.; Zhao, H. Y.; Tan, X.; Lin, S.; Yu, K. S.; Mu, X. Q.; Tao, Z.

H.; Ji, P. X.; Mu, S. C. Fe-S dually modulated adsorbate evolution and lattice oxygen compatible mechanism for water oxidation. *Nat. Commun.* **2024**, *15*, 8293.
[17] Zhao, J. W.; Zhang, H.; Li, C. F.; Zhou, X.; Wu, J. Q.; Zeng, F.; Zhang, J. W.; Li, G. R. Key roles of surface Fe sites and Sr vacancies in the perovskite for an efficient oxygen evolution reaction via lattice oxygen oxidation. *Energy Environ. Sci.* **2022**, *15*, 3912–3922.
[18] Yin, Z. H.; Huang, Y.; Song, K. P.; Li, T. T.; Cui, J. Y.; Meng, C.; Zhang, H. G.; Wang, J. J. Ir single atoms boost metal-oxygen covalency on selenide-derived NiOOH for direct intramolecular oxygen coupling. *J. Am. Chem. Soc.* **2024**, *146*, 6846–6855.
[19] Zhang, T.; Zhao, H. F.; Chen, Z. J.; Yang, Q.; Gao, N.; Li, L.; Luo, N.; Zheng, J.; Bao, S. D.; Peng, J. et al. High-entropy alloy enables multi-path electron synergism and lattice oxygen activation for enhanced oxygen evolution activity. *Nat. Commun.* **2025**, *16*, 3327.
[20] Deng, Q. M.; Li, H.; Pei, K.; Wong, L. W.; Zheng, X. D.; Tsang, C. S.; Chen, H. L.; Shen, W. Q.; Ly, T. H.; Zhao, J. et al. Strategic design for high-efficiency oxygen evolution reaction (OER) catalysts by triggering lattice oxygen oxidation in cobalt spinel oxides. *ACS Nano* **2024**, *18*, 33718–33728.
[21] Grimaud, A.; Diaz-Morales, O.; Han, B. H.; Hong, W. T.; Lee, Y. L.; Giordano, L.; Stoerzinger, K. A.; Koper, M. T. M.; Shao-Horn, Y. Activating lattice oxygen redox reactions in metal oxides to catalyse oxygen evolution. *Nat. Chem.* **2017**, *9*, 457–465.
[22] Wang, F. Q.; Zou, P. C.; Zhang, Y. Y.; Pan, W. L.; Li, Y.; Liang, L. M.; Chen, C.; Liu, H.; Zheng, S. J. Activating lattice oxygen in high-entropy LDH for robust and durable water oxidation. *Nat. Commun.* **2023**, *14*, 6019.
[23] Zhang, N.; Chai, Y. Lattice oxygen redox chemistry in solid-state electrocatalysts for water oxidation. *Energy Environ. Sci.* **2021**, *14*, 4647–4671.
[24] Zhao, J. W.; Li, C. F.; Shi, Z. X.; Guan, J. L.; Li, G. R. Boosting lattice oxygen oxidation of perovskite to efficiently catalyze oxygen evolution reaction by FeOOH decoration. *Research* **2020**, *2020*, 6961578.
[25] Li, B.; Tian, Z.; Li, L.; Wang, Y. H.; Si, Y.; Wan, H.; Shi, J. H.; Huang, G. F.; Hu, W. Y.; Pan, A. L. et al. Directional charge transfer channels in a monolithically integrated electrode for photoassisted overall water splitting. *ACS Nano* **2023**, *17*, 3465–3482.
[26] Wang, Y. H.; Li, L.; Shi, J. H.; Xie, M. Y.; Nie, J. H.; Huang, G. F.; Li, B.; Hu, W. Y.; Pan, A. L.; Huang, W. Q. Oxygen defect engineering promotes synergy between adsorbate evolution and single lattice oxygen mechanisms of OER in transition metal-based (oxy)hydroxide. *Adv. Sci.* **2023**, *10*, 2303321.
[27] Huang, Z. F.; Song, J. J.; Du, Y. H.; Xi, S. B.; Dou, S.; Nsanzimana, J. M. V.; Wang, C.; Xu, Z. J.; Wang, X. Chemical and structural origin of lattice oxygen oxidation in Co–Zn oxyhydroxide oxygen evolution electrocatalysts. *Nat. Energy* **2019**, *4*, 329–338.
[28] Qian, Z. X.; Liang, G. H.; Shen, L. F.; Zhang, G.; Zheng, S. S.; Tian, J. H.; Li, J. F.; Zhang, H. Phase engineering facilitates O–O coupling via lattice oxygen mechanism for enhanced oxygen evolution on nickel-iron phosphide. *J. Am. Chem. Soc.* **2025**, *147*, 1334–1343.
[29] He, Z. Y.; Zhang, J.; Gong, Z. H.; Lei, H.; Zhou, D.; Zhang, N.; Mai, W.; Zhao, S. J.; Chen, Y. Activating lattice oxygen in NiFe-based (oxy)hydroxide for water electrolysis. *Nat. Commun.* **2022**, *13*, 2191.
[30] Gu, M. Z.; Jiang, L.; Wang, H.; Chen, Q.; Hao, Y. X.; Li, L. L.; Hu, F.; Zhang, X. J.; Wu, Y. P.; Wang, G. F. et al. Iodine-induced redirection of active sources in Cu-based catalysts during efficient and stable water oxidation. *J. Am. Chem. Soc.* **2025**, *147*, 19675–19686.
[31] Wang, F. Q.; Feng, L.; Zhang, M. W.; Cong, H. L. Engineering oxygen nonbonding states in high entropy hydroxides for scalable water oxidation. *Nat. Commun.* **2025**, *16*, 6624.
[32] Jia, C. H.; Chen, Y.; Zhou, C. Y.; Xiang, X. P.; Long, X.; Zhao, B.; Zhang, N.; Zhao, S. J.; Chai, L. Y.; Liu, X. M. et al. Oxide heterostructure engineering drives stable lattice oxygen evolution for highly efficient and robust water electrolysis. *ACS Nano* **2025**, *19*, 19938–19950.
[33] Xin, S. S.; Tang, Y.; Jia, B. H.; Zhang, Z. F.; Li, C. P.; Bao, R.; Li, C. J.; Yi, J. H.; Wang, J. S.; Ma, T. Y. Coupling adsorbed evolution and lattice oxygen mechanism in Fe–$Co(OH)_2$/Fe_2O_3 heterostructure for enhanced electrochemical water oxidation. *Adv. Funct. Mater.* **2023**, *33*, 2305243.
[34] Wang, X. P.; Zhong, H. Y.; Xi, S. B.; Lee, W. S. V.; Xue, J. M. Understanding of oxygen redox in the oxygen evolution reaction. *Adv. Mater.* **2022**, *34*, 2107956.
[35] Haynes, W. M. *CRC Handbook of Chemistry and Physics: A Ready-Reference Book of Chemical and Physical*; CRC Press: Boca Raton, 2012.
[36] Sun, H. C.; Zhang, W.; Li, J. G.; Li, Z. S.; Ao, X.; Xue, K. H.; Ostrikov, K. K.; Tang, J.; Wang, C. D. Rh-engineered ultrathin NiFe-LDH nanosheets enable highly-efficient overall water splitting and urea electrolysis. *Appl. Catal. B: Environ.* **2021**, *284*, 119740.
[37] Liang, H. F.; Gandi, A. N.; Xia, C.; Hedhili, M. N.; Anjum, D. H.; Schwingenschlögl, U.; Alshareef, H. N. Amorphous NiFe-OH/NiFeP electrocatalyst fabricated at low temperature for water oxidation applications. *ACS Energy Lett.* **2017**, *2*, 1035–1042.
[38] Hui, L.; Xue, Y. R.; Huang, B. L.; Yu, H. D.; Zhang, C.; Zhang, D. Y.; Jia, D. Z.; Zhao, Y. J.; Li, Y. J.; Liu, H. B. et al. Overall water splitting by graphdiyne-exfoliated and -sandwiched layered double-hydroxide nanosheet arrays. *Nat. Commun.* **2018**, *9*, 5309.
[39] Boppella, R.; Tan, J.; Yang, W.; Moon, J. Homologous CoP/NiCoP heterostructure on N-doped carbon for highly efficient and pH-universal hydrogen evolution electrocatalysis. *Adv. Funct. Mater.* **2019**, *29*, 1807976.
[40] Xu, H. B.; Fei, B.; Cai, G. H.; Ha, Y.; Liu, J.; Jia, H. X.; Zhang, J. C.; Liu, M.; Wu, R. B. Boronization-induced ultrathin 2D nanosheets with abundant crystalline-amorphous phase boundary supported on nickel foam toward efficient water splitting. *Adv. Energy Mater.* **2020**, *10*, 1902714.
[41] Gao, Y.; Qiao, Y. H.; Li, X. R.; Huang, C. Y.; Zhang, J.; Wang, Y. R.; Zou, X. L.; Xia, Z. H.; Yang, X. X.; Lu, X. G. et al. Bimetallic site substitution of NiCoP nanoneedles as bifunctional electrocatalyst for boosted water splitting. *Nano Res.* **2024**, *17*, 9540–9549.
[42] Dong, Z. H.; Lin, F.; Yao, Y. H.; Jiao, L. F. Crystalline $Ni(OH)_2$/amorphous $NiMoO_x$ mixed-catalyst with Pt-like performance for hydrogen production. *Adv. Energy Mater.* **2019**, *9*, 1902703.
[43] Xu, Q.; Wang, P. C.; Wan, L.; Xu, Z. A.; Sultana, M. Z.; Wang, B. G. Superhydrophilic/superaerophobic hierarchical NiP_2@MoO_2/Co(Ni)MoO_4 core–shell array electrocatalysts for efficient hydrogen production at large current densities. *ACS Appl. Mater. Interfaces* **2022**, *14*, 19448–19458.
[44] Wu, Z. P.; Zuo, S. W.; Pei, Z. H.; Zhang, J.; Zheng, L. R.; Luan, D. Y.; Zhang, H. B.; Lou, X. W. *Operando* unveiling the activity origin via preferential structural evolution in Ni-Fe (oxy)phosphides for efficient oxygen evolution. *Sci. Adv.* **2025**, *11*, eadu5370.
[45] Wang, Y. H.; Li, S. Q.; Hou, X.; Cui, T. T.; Zhuang, Z. C.; Zhao, Y. H.; Wang, H. Z.; Wei, W.; Xu, M.; Fu, Q. et al. Low-spin Fe^{3+} evoked by multiple defects with optimal intermediate adsorption attaining unparalleled performance in water oxidation. *Adv. Mater.* **2024**, *36*, 2412598.
[46] Huang, L. C.; Yao, R. Q.; Wang, X. Q.; Sun, S.; Zhu, X. X.; Liu, X. H.; Kim, M. G.; Lian, J. S.; Liu, F. Z.; Li, Y. Q. et al. *In situ* phosphating of Zn-doped bimetallic skeletons as a versatile electrocatalyst for water splitting. *Energy Environ. Sci.* **2022**, *15*, 2425–2434.
[47] Li, C. F.; Xie, L. J.; Zhao, J. W.; Gu, L. F.; Tang, H. B.; Zheng, L. R.; Li, G. R. Interfacial Fe−O−Ni−O−Fe bonding regulates the active Ni sites of Ni-MOFs via iron doping and decorating with FeOOH for super-efficient oxygen evolution. *Angew. Chem., Int. Ed.* **2022**, *61*, e202116934.
[48] Pan, Y.; Sun, K. A.; Liu, S. J.; Cao, X.; Wu, K. L.; Cheong, W. C.; Chen, Z.; Wang, Y.; Li, Y.; Liu, Y. Q. et al. Core–shell ZIF-8@ZIF-67-derived CoP nanoparticle-embedded N-doped carbon nanotube hollow polyhedron for efficient overall water splitting. *J. Am. Chem. Soc.* **2018**, *140*, 2610–2618.
[49] Yang, L.; Liu, R. M.; Jiao, L. F. Electronic redistribution:

Construction and modulation of interface engineering on CoP for enhancing overall water splitting. *Adv. Funct. Mater.* **2020**, *30*, 1909618.
[50] Hu, X. M.; Zhang, S. L.; Sun, J. W.; Yu, L.; Qian, X. Y.; Hu, R. D.; Wang, Y. N.; Zhao, H.; Zhu, J. W. 2D Fe-containing cobalt phosphide/cobalt oxide lateral heterostructure with enhanced activity for oxygen evolution reaction. *Nano Energy* **2019**, *56*, 109–117.
[51] Sun, Z. Z.; Curto, A.; Rodríguez-Fernández, J.; Wang, Z. G.; Parikh, A.; Fester, J.; Dong, M. D.; Vojvodic, A.; Lauritsen, J. V. The effect of Fe dopant location in Co(Fe)OOH$_x$ nanoparticles for the oxygen evolution reaction. *ACS Nano* **2021**, *15*, 18226–18236.
[52] Briega-Martos, V.; Guzman-Soriano, R.; Jiang, J. H.; Yang, Y. The (mis)uses of Tafel slope. *Nat. Catal.* **2025**, *8*, 863–866.
[53] Tafel, J. Über die Polarisation bei kathodischer Wasserstoffentwicklung. *Z. Phys. Chem*. **1905**, *50U*, 641–712.
[54] Gomez, R.; Fernandez-Vega, A.; Feliu, J. M.; Aldaz, A. Hydrogen evolution on platinum single crystal surfaces: Effects of irreversibly adsorbed bismuth and antimony on hydrogen adsorption and evolution on platinum (100). *J. Phys. Chem.* **1993**, *97*, 4769–4776.
[55] Anderson, A. B.; Albu, T. V. *Ab initio* determination of reversible potentials and activation energies for outer-sphere oxygen reduction to water and the reverse oxidation reaction. *J. Am. Chem. Soc.* **1999**, *121*, 11855–11863.
[56] Holewinski, A.; Linic, S. Elementary mechanisms in electrocatalysis: Revisiting the ORR Tafel slope. *J. Electrochem. Soc.* **2012**, *159*, H864–H870.
[57] Qiao, Y. Y.; Pan, Y. Q.; Zhang, J. W.; Wang, B.; Wu, T. T.; Fan, W. J.; Cao, Y. C.; Mehmood, R.; Zhang, F.; Zhang, F. X. Multiple carbon interface engineering to boost oxygen evolution of NiFe nanocomposite electrocatalyst. *Chin. J. Catal.* **2022**, *43*, 2354–2362.
[58] Zheng, X. R.; Han, X. P.; Cao, Y. H.; Zhang, Y.; Nordlund, D.; Wang, J. H.; Chou, S. L.; Liu, H.; Li, L. L.; Zhong, C. et al. Identifying dense $NiSe_2$/$CoSe_2$ heterointerfaces coupled with surface high-valence bimetallic sites for synergistically enhanced oxygen electrocatalysis. *Adv. Mater.* **2020**, *32*, 2000607.
[59] Han, H.; Choi, H.; Mhin, S.; Hong, Y. R.; Kim, K. M.; Kwon, J.; Ali, G.; Chung, K. Y.; Je, M.; Umh, H. N. et al. Advantageous crystalline-amorphous phase boundary for enhanced electrochemical water oxidation. *Energy Environ. Sci.* **2019**, *12*, 2443–2454.
[60] Duan, Y.; Yu, Z. Y.; Hu, S. J.; Zheng, X. S.; Zhang, C. T.; Ding, H. H.; Hu, B. C.; Fu, Q. Q.; Yu, Z. L.; Zheng, X. et al. Scaled-up synthesis of amorphous NiFeMo oxides and their rapid surface reconstruction for superior oxygen evolution catalysis. *Angew. Chem., Int. Ed.* **2019**, *58*, 15772–15777.
[61] Bodappa, N.; Su, M.; Zhao, Y.; Le, J. B.; Yang, W. M.; Radjenovic, P.; Dong, J. C.; Cheng, J.; Tian, Z. Q.; Li, J. F. Early stages of electrochemical oxidation of Cu(111) and polycrystalline Cu surfaces revealed by *in situ* Raman spectroscopy. *J. Am. Chem. Soc.* **2019**, *141*, 12192–12196.
[62] Lee, S.; Chu, Y. C.; Bai, L. C.; Chen, H. M.; Hu, X. L. Operando identification of a side-on nickel superoxide intermediate and the mechanism of oxygen evolution on nickel oxyhydroxide. *Chem Catal.* **2023**, *3*, 100475.
[63] Zhu, Y.; Wang, X.; Zhu, X. H.; Wu, Z. X.; Zhao, D. S.; Wang, F.; Sun, D. M.; Tang, Y. W.; Li, H.; Fu, G. T. Improving the oxygen evolution activity of layered double-hydroxide via erbium-induced electronic engineering. *Small* **2023**, *19*, 2206531.
[64] Bai, S. Z.; Dai, W. J.; Chen, X.; Zhang, F.; Chen, W. G.; Wu, B.; Zhao, C. J.; Guo, J.; Huang, S. F. Surface-reconstructed nanoporous (CoNiFe)OOH modulated by $Zn(OH)_4^{2-}$ anions: A synergistic strategy for enhanced oxygen evolution reaction electrocatalysis. *Nano Res.* **2025**, *18*, 94907809.
[65] Wu, H.; Fu, Z. Z.; Chang, J. W.; Hu, Z. A.; Li, J.; Wang, S. Y.; Yu, J. K.; Yong, X.; Waterhouse, G. I. N.; Tang, Z. Y. et al. Engineering high-density microcrystalline boundary with V-doped RuO_2 for high-performance oxygen evolution in acid. *Nat. Commun.* **2025**, *16*, 4482.
[66] Zhang, N.; Hu, Y.; An, L.; Li, Q. Y.; Yin, J.; Li, J. Y.; Yang, R.; Lu, M.; Zhang, S.; Xi, P. X. et al. Surface activation and Ni–S stabilization in NiO/NiS_2 for efficient oxygen evolution reaction. *Angew. Chem., Int. Ed.* **2022**, *61*, e202207217.
[67] Sun, X. G.; Shen, W.; Liu, H.; Xi, P. X.; Jaroniec, M.; Zheng, Y.; Qiao, S. Z. Corrosion-resistant NiFe anode towards kilowatt-scale alkaline seawater electrolysis. *Nat. Commun.* **2024**, *15*, 10351.
[68] Zhang, Q.; Xiao, W.; Fu, H. C.; Li, X. L.; Lei, J. L.; Luo, H. Q.; Li, N. B. Unraveling the mechanism of self-repair of NiFe-based electrocatalysts by dynamic exchange of iron during the oxygen evolution reaction. *ACS Catal.* **2023**, *13*, 14975–14986.
[69] Wang, S. W.; Lin, B. B.; Qi, M. H.; Chen, J. D.; Du, X. B. W.; Mao, S. J.; Wang, Y. Cerium-doped NiFe hydroxides enabling hybrid pathways for durable alkaline water oxidation under fluctuating power. *ACS Nano* **2025**, *19*, 31915–31928.
[70] Yao, Y. C.; Hu, S. L.; Chen, W. X.; Huang, Z. Q.; Wei, W. C.; Yao, T.; Liu, R. R.; Zang, K. T.; Wang, X. Q.; Wu, G. et al. Engineering the electronic structure of single atom Ru sites via compressive strain boosts acidic water oxidation electrocatalysis. *Nat. Catal.* **2019**, *2*, 304–313.
[71] Xu, J.; Jin, H. Y.; Lu, T.; Li, J. S.; Liu, Y.; Davey, K.; Zheng, Y.; Qiao, S. Z. $IrO_x \cdot nH_2O$ with lattice water-assisted oxygen exchange for high-performance proton exchange membrane water electrolyzers. *Sci. Adv.* **2023**, *9*, eadh1718.
[72] Sheng, Q.; Li, X.; Prins, R.; Liu, C. J.; Hao, Q. L.; Chen, S. Z. Understanding the reduction of transition-metal phosphates to transition-metal phosphides by combining temperature-programmed reduction and infrared spectroscopy. *Angew. Chem., Int. Ed.* **2021**, *60*, 11180–11183.
[73] Sugawara, Y.; Nakase, Y.; Anilkumar, G. M.; Kamata, K.; Yamaguchi, T. Oxygen evolution activity of nickel-based phosphates and effects of their electronic orbitals. *Nanoscale Adv.* **2025**, *7*, 456–466.
[74] Jastrzębski, W.; Sitarz, M.; Rokita, M.; Bułat, K. Infrared spectroscopy of different phosphates structures. *Spectrochim. Acta Part A: Mol. Biomol. Spectrosc.* **2011**, *79*, 722–727.
[75] Wang, J.; Zhang, M. K.; Yang, G. L.; Song, W. W.; Zhong, W. T.; Wang, X. Y.; Wang, M. M.; Sun, T. M.; Tang, Y. F. Heterogeneous bimetallic Mo–NiP_x/NiS_y as a highly efficient electrocatalyst for robust overall water splitting. *Adv. Funct. Mater.* **2021**, *31*, 2101532.
[76] Yu, X. Y.; Feng, Y.; Guan, B. Y.; Lou, X. W.; Paik, U. Carbon coated porous nickel phosphides nanoplates for highly efficient oxygen evolution reaction. *Energy Environ. Sci.* **2016**, *9*, 1246–1250.
[77] Zhao, J. W.; Yue, K. H.; Zhang, H.; Wei, S. Y.; Zhu, J. W.; Wang, D. D.; Chen, J. Z.; Fominski, V. Y.; Li, G. R. The formation of unsaturated IrO_x in $SrIrO_3$ by cobalt-doping for acidic oxygen evolution reaction. *Nat. Commun.* **2024**, *15*, 2928.
[78] Xin, H. L.; Linic, S. Communications: Exceptions to the d-band model of chemisorption on metal surfaces: The dominant role of repulsion between adsorbate states and metal *d*-states. *J. Chem. Phys.* **2010**, *132*, 221101.
[79] Imanishi, A.; Okamura, T.; Ohashi, N.; Nakamura, R.; Nakato, Y. Mechanism of water photooxidation reaction at atomically flat TiO_2 (rutile) (110) and (100) surfaces: Dependence on solution pH. *J. Am. Chem. Soc.* **2007**, *129*, 11569–11578.
[80] Liu, J. Y.; Wang, T. Y.; Sun, M. Z.; Liao, M. Y.; Wang, S. Y.; Liu, S. X.; Shi, H.; Liu, Y.; Shen, Y.; Cao, R. G. et al. Triggering the dual-metal-site lattice oxygen mechanism with *in situ*-generated Mn^{3+} sites for enhanced acidic oxygen evolution. *J. Am. Chem. Soc.* **2024**, *146*, 33276–33287.